Ni Nanoparticles on CeO_2(111): Energetics, Electron Transfer and Structure by Ni Adsorption Calorimetry, Spectroscopies and DFT

Zhongtian Mao[†⊥], Pablo G. Lustemberg[‡§⊥], John R. Rumptz[†], M. Verónica Ganduglia-Pirovano[§*] and Charles T. Campbell[†*]

[†]Department of Chemistry, University of Washington, Seattle, Washington 98195-1700, USA

[‡]Instituto de Física Rosario (IFIR-CONICET) and Universidad Nacional de Rosario (UNR), Ocampo y Esmeralda, S2000EKF Rosario, Santa Fe, Argentina

[§]Instituto de Catálisis y Petroleoquímica (ICP-CSIC), C/Marie Curie 2, 28049 Madrid, Spain

Abstract

The morphology, interfacial bonding energetics and charge transfer of Ni clusters and nanoparticles on slightly-reduced CeO_{2-x}(111) surfaces at 100 to 300 K have been studied using single crystal adsorption calorimetry (SCAC), low-energy ion scattering spectroscopy (LEIS), X-ray photoelectron spectroscopy (XPS), low energy electron diffraction (LEED) and density functional theory (DFT). The initial heat of adsorption of Ni vapor decreased with the extent of pre-reduction (x) of the CeO_{2-x}(111), showing that stoichiometric ceria adsorbs Ni more strongly than oxygen vacancies. On $CeO_{1.95}$(111) at 300 K, the heat dropped quickly with coverage in the first 0.1 ML, attributed to nucleation of Ni clusters on stoichiometric steps, followed by the Ni particles spreading onto less favorable terrace sites. At 100 K, the clusters nucleate on terraces due to slower diffusion. Adsorbed Ni monomers are in the +2 oxidation state, and they bind by ~45 kJ/mol more strongly to step sites than terraces. The measured heat of adsorption versus average particle size on terraces is favorably compared to DFT calculations. The Ce 3d XPS lineshape showed an increase in Ce^{3+}/Ce^{4+} ratio with Ni coverage, providing the number of electrons donated to the ceria per Ni atom. The charge transferred per Ni is initially large but strongly decreases with increasing cluster size for both experiments and DFT, and shows large differences between clusters at steps versus terraces. This charge is localized on the interfacial Ni and Ce atoms in their atomic layers closest to the interface. This knowledge is crucial to understanding the nature of the active sites on the surface of Ni-CeO_2 catalysts for which metal-oxide interactions play a very important role in the activation of O–H and C–H bonds. The changes in these interactions with Ni particle size (metal loading) and the extent of reduction of the ceria help to explain how previously reported catalytic activity and selectivity change with these same structural details.

* Corresponding authors: Charles T. Campbell: charliec@uw.edu
and M. Verónica Ganduglia-Pirovano: vgp@icp.csic.es

[⊥] These authors have contributed equally to this work.

Keywords: catalyst, nickel / ceria, nanoparticles, size effect, metal adsorption, calorimetry, DFT.

1. Introduction

Nickel supported on CeO_2 is an important catalyst material with promise in a wide variety of applications,[1-17] perhaps most importantly in the direct conversion of methane to methanol.[14] Ceria is a widely-used support material for late transition metal catalysts, [18-20] and is well known to enhance the stability of supported metals to resist deactivation by sintering.[18, 19, 21-24] The (111) face of CeO_2 is the most studied and well-understood among the low-index faces of ceria in terms of structure and reactivity. Thus the interaction of Ni with the CeO_2(111) surface is of fundamental interest in catalysis. Recent works have shown that Ni-ceria interactions are crucial to achieving high catalytic performance.[6,10-12,14] In particular, it has been found that oxidized Ni species (Ni^{2+}) at the Ni-ceria interface that result from the transfer of two 4*s* electrons from Ni to the empty 4*f* band of ceria, generating two Ce^{3+} ions, activate O–H and C–H bonds at room temperature. Moreover, the metal loading has a drastic effect on the catalytic properties. For example, as the coverage of Ni increases and 3D nanoparticles form, the dissociation of O–H bonds is hindered on the Ni atoms that are not in direct contact with the ceria support,[6] and the ability of the system to dissociate methane is also hindered due to the formation of NiC_x on the surface. [11] Because the strong electronic perturbations in chemisorbed Ni species on ceria, which produce dramatic changes in their chemical properties, are extremely sensitive to the coverage of Ni on the ceria substrate, it is crucial to understand how the structure, heat of adsorption, and the amount of Ni→ ceria charge transfer changes with Ni coverage.

Here we study the morphology and interfacial energetics of vapor-deposited Ni on slightly-reduced CeO_2(111) surfaces using metal vapor adsorption calorimetry, surface analysis techniques and density functional theory. The results reveal that Ni grows as 3-dimensional particles and clarify electronic details of the Ni - CeO_2 interactions. The results show that the heat of Ni adsorption and the number of electrons donated to the ceria per Ni atom change strongly as the size of the Ni clusters grows and with the extent of reduction of the ceria support, and that the Ni clusters bind more weakly to (111) terrace sites than to step edges.

These results help explain the unique properties of ceria as a support for Ni nanoparticle catalysts.

2. Methods

2.1. Experimental Methods

The apparatus and methods for SCAC, XPS, LEIS and LEED have described in detail previously.[25-28]

The CeO_{2-x}(111) thin films (x = 0.05 and 0.2) were grown on a clean Pt(111) single crystal surface up to a thickness of 4 nm, using the same methods as described previously that were shown to produce ordered (111) terraces with ~5% step sites.[29] This is thick enough to give a bulk-like behavior based on the adsorption energy of Ag vapor.[29] A sharp (1.4×1.4) LEED pattern was observed for the as-grown CeO_{2-x}(111) films, indicating the surface was well ordered and the epitaxial relationship with the underlying Pt was in agreement with prior reports.[30] The Ce oxidation states were characterized with XPS based on lineshape fitting of the Ce 3d peaks as described previously[26].

Metal vapor adsorption calorimetry was performed as described previously.[25] In brief, a pyroelectric polyvinylidene fluoride (PVDF) ribbon is pressed against the backside of a 1-□m-thick Pt(111) single crystal sample as the heat detector. During SCAC, a well-defined 4.26 mm diameter beam of Ni atoms is generated from an e-beam evaporator, collimated through a series of apertures, chopped into 100 ms pulses with a period of 2 s, and finally dosed onto the sample. The heat release during the adsorption of Ni atoms is detected by the PVDF ribbon. For each calorimetry run, the heat detector response is calibrated by pulses from a HeNe laser with known energy. To subtract the signal from thermal radiation, the sample is blocked by a BaF_2 window that only allows a known fraction of radiation to penetrate. The signal measured associated with the radiation is corrected with the BaF_2 transmission and subtracted from the total heat signal, to leave only the part that is due to Ni vapor adsorption. As we always do in SCAC,[31] this heat is corrected for the difference in the metal vapor's internal energy (2RT in a directed beam) between the metal vapor source temperature (~2000 K) and the surface temperature (100 or 300 K), so that the heats reported below are equal to the negative of the standard enthalpy of Ni adsorption at the surface temperature.

The flux of Ni atoms is measured with an on-axis quartz crystal microbalance (QCM) and an off-axis QCM. The off-axis QCM facing directly to the e-beam evaporator monitors the flux throughout the whole experiment. The on-axis QCM is placed at the sample position only before

and after the adsorption calorimetry. The beginning and ending fluxes measured by the on-axis QCM are used to scale the off-axis QCM fluxes so that it provides the Ni flux at the sample position for all times during the calorimetry.[25] The sticking probability of each pulse is measured simultaneously with its heat using a modified King and Well's method.[25] Combining the flux and the sticking probability, we calculate the amount of Ni atoms that stick to the sample in each pulse. The differential heat of adsorption versus the cumulative coverage of Ni is thus available. The Ni coverages are reported here in monolayers (ML), where 1 ML is defined as 7.89×10^{14} atoms per cm^2, which is the areal density of coordinatively-unsaturated O atoms on the ideal bulk-terminated $CeO_2(111)$ surface.

The growth morphology of adsorbed Ni on $CeO_{2-x}(111)$ was determined using He^+ low energy ion scattering (LEIS) with an incident angle of 45˚ from normal and a scattering angle of 135˚. The normalized LEIS signals give the fraction of surface area that is covered by Ni nanoparticles.[32]

2.2. Computational Methods

All electronic structure calculations were carried out using the spin-polarized DFT approach as implemented in the Vienna ab initio simulation package (VASP) {vasp site, http://www.vasp.at; version vasp.5.3.5}[33, 34] Ce (4f, 5s, 5p, 5d, 6s), O (2s, 2p), and Ni (3p,3d,4s) electrons were explicitly treated as valence states within the projector augmented wave (PAW) method[35] with a plane-wave cutoff energy of 415 eV, whereas the remaining electrons were considered as part of the atomic core. Total energies and forces were calculated with a precision of 10^{-6} eV and 10^{-2} eV/Å for electronic and force convergence, respectively, within the DFT+U approach by Dudarev et al.[36] ($U_{eff} = U - J = 4.5$ eV for the Ce 4*f* electrons) with the generalized gradient approximation (GGA) proposed by Perdew, Burke, and Ernzerhof (PBE).[37] We note that questions regarding the best value for the U parameter are still under debate.[38-40] Nonetheless, most DFT+U studies of reduced ceria-based systems agree that U values in the range of 4.5–6.0 eV with GGA are suitable for the description of the localization of charge driving the $Ce^{4+} \rightarrow Ce^{3+}$ reduction. However, one should bear in mind that there is in general no unique U that gives a reasonable account of all systems' properties.[41-43] Long-range dispersion corrections were also considered, employing the so-called DFT-D3 approach.[44, 45]

3. Results

3.1. Ni Sticking Probability on CeO_{2-x}(111)

The sticking probability was measured using the signal for non-sticking Ni gas atoms in each pulse detected with the transient QMS signal for Ni gas, normalized to the signal for the reference zero-sticking pulse from a hot W flag, where no permanent sticking occurs. For all three systems we studied ($CeO_{1.95}$(111) at 300 K, $CeO_{1.8}$(111) at 300 K, $CeO_{1.95}$(111) at 100 K), the sticking probability started at ~97% and increased to unity within the first 0.5 ML.

3.2. Ni Growth Morphology on CeO_{2-x}(111)

Gaseous Ni was deposited onto CeO_{2-x}(111) films at 300 and 100 K in discrete amounts. The Ni and Ce signals in He^+ LEIS were monitored after each such Ni dose. The integrated Ni signals were normalized to the signal from a thick Ni overlayer (>10 nm average thickness). The Ce signals were normalized to those for a clean CeO_{2-x}(111) surface taken at the beginning of each experiment. The normalized Ni LEIS signal gives the fraction of surface covered and shadowed by Ni nanoparticles, and the normalized Ce signals give the fraction of surface which is not masked by Ni. The normalized Ni and Ce LEIS signal data are plotted versus Ni coverage in Figure 1 and compared with two typical growth models. The straight dashed lines correspond to the normalized LEIS signal that would be expected if Ni grew in a layer-by-layer mode. They do not fit well with the measured LEIS data. The solid curved lines correspond to 3-dimensional (3D) growth mode assuming the Ni grows as 3D particles with the shape of flat disks with a constant aspect ratio (height / diameter) of 0.25 on $CeO_{1.95}$(111) and 0.20 on $CeO_{1.8}$(111), as suggested by STM studies.[46] In the flat-disk model, we assume that the Ni particles all have this same shape at all coverages and the same size at any given coverage, and the particle number density *n* does not change with metal coverage (i.e., the saturation number density of nuclei is reached by the first dose, as is generally the case for such systems[47]). This model is applied only up to the coverage where ~35% of the surface is covered by particles, since particles overlap with each other at higher area fraction. Previous work showed that, if the particles grow as hemispherical caps, the total surface area masked by particles in the LEIS signals for the incident and detection angles used here is 1.207 times the metal/support interfacial area, due to a shadowing effect.[32] This ratio, calculated in the same way, is changed to 1.318 for $CeO_{1.95}$(111) and 1.255 for $CeO_{1.8}$(111) based on their flat-disk aspect ratios (height/diameter = 0.25 and 0.20, respectively). With these

assumptions, the particle number density *n* is the only fitting parameter in the equation, and it is determined from the best fitting line in Figure 1.

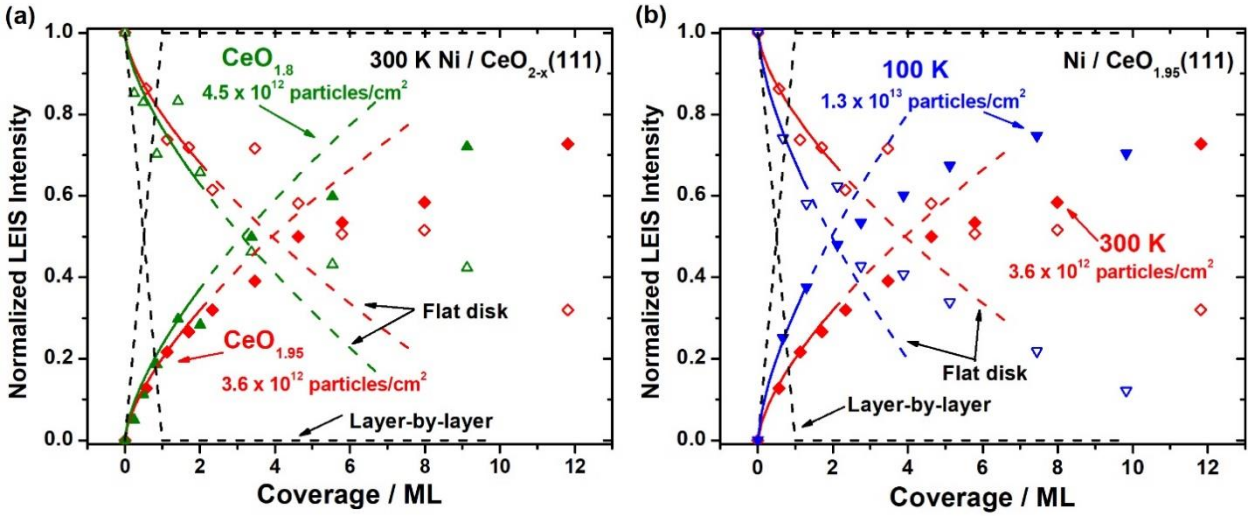

Figure 1. (a) Integrated Ni (closed symbols) and Ce (open symbols) LEIS signal intensities (normalized to thick multilayer Ni and clean CeO_{2-x}(111), respectively) as a function of Ni coverage after deposition onto (a) $CeO_{1.95}$(111) (red diamonds) and $CeO_{1.8}$(111) (green triangles) at 300 K (b) $CeO_{1.95}$(111) at 300 K (red diamonds) and 100 K (blue triangles). The black dashed lines correspond to the normalized LEIS signal that would be observed if Ni grew in a layer-by-layer fashion, while the colored solid lines correspond to Ni growing as flat disks with a fixed aspect ratio (0.25 on $CeO_{1.95}$ and 0.20 on $CeO_{1.8}$) and a fixed particle density of 3.6×10^{12} particles/cm^2 (red), 4.5×10^{12} particles/cm^2 (green) and 1.3×10^{13} particles/cm^2 (blue). This model is only reasonable up to ~35% of the surface is covered, since particles will soon start to overlap with each other at higher coverage. The colored dashed lines after that are only a guide to the eye.

Following this approach, the flat-disk model gives a good fit to the LEIS data as shown in Figure 1, and the best-fit particle number densities on CeO_{2-x}(111) at 300 and 100 K are shown. The extent of reduction of the ceria has only a minor effect on the Ni particle density. At 300 K, it was 3.6×10^{12} particles/cm^2 on $CeO_{1.95}$(111), and 4.5×10^{12} particles/cm^2 on $CeO_{1.8}$(111). A similar small increase in the particle density with extent of reduction was reported based on STM images.[48] Comparing the growth of Ni on $CeO_{1.95}$(111) at 300 and 100 K, a huge temperature effect was observed. The Ni particle density on $CeO_{1.95}$(111) was 1.3×10^{13} particles/cm^2 at 100 K, about 4-fold higher than at 300 K.

3.3. Heat of Adsorption of Ni on CeO_{2-x}(111)

The heat of adsorption of Ni gas atoms on CeO_{2-x}(111) for x = 0.05 and 0.2 at 300 K and for x = 0.05 at 100 K are plotted in Figure 2 as a function of Ni coverage. At 300 K on $CeO_{1.95}$(111),

Ni has an initial heat of adsorption of 345 kJ/mol, and it decreases rapidly to 323 kJ/mol by 0.2 ML. The heat then increases, slowly approaching the sublimation heat of bulk Ni at 430 kJ/mol by 9 ML. This type of reverse in slope with coverage has been seen before and attributed to the adsorption of metal adatoms to stronger-binding defects (step edges) at the lowest coverage that become saturated as coverage increases.[26] Thus, the initial heat of 345 kJ/mol on $CeO_{1.95}$(111) is attributed to Ni adsorption at step edges. The minimum heat occurs at 0.1-0.2 ML Ni, which is consistent with the step-site density of ~5% of the total sites, given that some Ni atoms will bind to other Ni atoms in clusters rather than directly at step sites as the step sites approach saturation by Ni atoms. On $CeO_{1.8}$(111), where the degree of reduction is larger and there are many more O vacancies, the initial heat at 300 K is 65 kJ/mol lower than for $CeO_{1.95}$(111) (280 vs 345 kJ/mol), and the heat remains lower up to ~0.2 ML. This clearly shows that Ni atoms do *not* prefer oxygen vacancies on CeO_2(111), the opposite as we observed for Ag and Au adsorption,[28, 29] but the same as for Cu.[26] This is consistent with the fact that Cu and Ni are much more oxophilic than Ag and Au, so they prefer to bind to the surface O atoms. The stronger binding of Au and Ag atoms to oxygen vacancies than that to stoichiometric terrace sites was also predicted by DFT calculations[49-54] and confirmed experimentally[55-58] in previous literature, though the decoration of oxygen vacancies by Au atoms has been challenged by recent STM experiments.[54] On $CeO_{1.8}$(111), there is no minimum in the heat of Ni adsorption versus coverage of the type seen on $CeO_{1.95}$(111) here. We attribute this to the preferential loss of the step-edge oxygen atoms (by far the least stable type of lattice O[59]) upon reduction, so that the step edges on $CeO_{1.8}$(111) no longer have enough O atoms to make more stable sites for Ni than stoichiometric terrace sites.

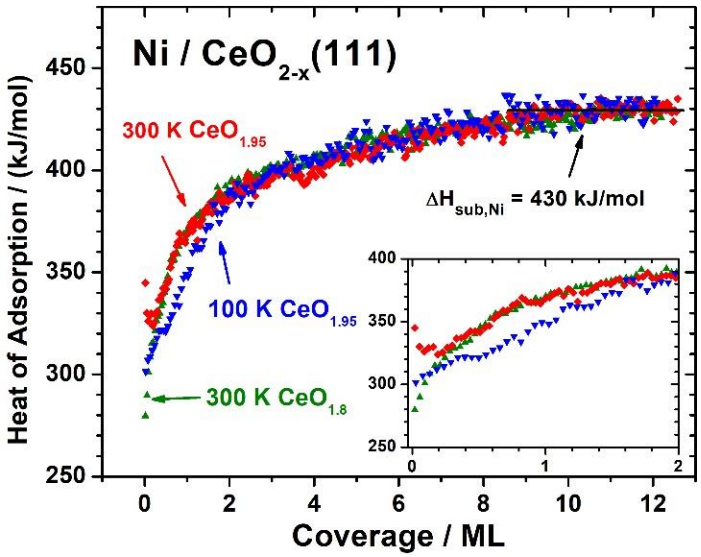

Figure 2. Differential heat of Ni atom adsorption on $CeO_{1.95}$(111) at 300 K (red diamonds), $CeO_{1.8}$(111) at 300 K (green triangles) and $CeO_{1.95}$(111) at 100 K (blue triangles), as a function of Ni coverage. 1 ML is defined as $7.89\times10^{18}/m^2$ which is the areal density of coordinatively-unsaturated O atoms on the ideal bulk-terminated CeO_2(111) surface.

At 100 K, the heat of Ni adsorption on $CeO_{1.95}$(111) is initially 45 kJ/mol lower than that at 300 K, and remains lower until 2 ML. There is also no minimum in heat versus coverage of the type seen at 300 K. We attribute this to the lack of mobility of the metal adatoms at 100 K so that they cannot diffuse to the stronger-binding step sites as they do at 300 K, and thus remain on terrace sites and nucleate particles there instead.

Dividing the Ni particle number density from the flat-disk model fit to Figure 1 (particles/cm^2) by the Ni coverage (atoms/cm^2), gives the average number of Ni atoms per particle at each coverage. Assuming these particles have the same density as bulk Ni(s), gives the volume per particle. Combining this volume with the disk shape (aspect ratio stated above) also gives the average Ni particle (flat disk) diameter at each coverage. Using this approach, the heat-versus-coverage data in Figure 2 have been replotted as Ni heat of adsorption vs the average Ni particle (flat-disk) diameter, as shown in Figure 3a.

Figure 3a shows the heat of Ni adsorption versus particle diameter on $CeO_{1.95}$(111) at 300 K and 100 K and $CeO_{1.8}$(111) at 300 K. At 300 K, the heat of Ni adsorption on Ni nanoparticles smaller than 1.5 nm in diameter supported on $CeO_{1.95}$(111) is higher than that on Ni nanoparticles supported on $CeO_{1.8}$(111), indicating that Ni does not bind more strongly to oxygen vacancies on

this surface. Above 1.5 nm diameter, the extent of reduction of CeO_{2-x} does not show a significant influence on the heat of Ni adsorption onto Ni nanoparticles. The plot for $CeO_{1.95}$(111) at 100 K stops at 1.5 nm diameter because the fractional surface area masked by Ni nanoparticles reaches ~35% here, and the flat-disk model used to fit the LEIS data is no longer appropriate at higher coverages. The heat of Ni adsorption on $CeO_{1.95}$(111) at 100 K for a given particle diameter below 1.3 nm is lower than the value for $CeO_{1.95}$(111) at 300 K. At 0.6 nm diameter, the difference is ~40 kJ/mol. We attribute this difference to the nucleation of Ni particles at step edges, where they bind more strongly than on CeO_2(111) terraces (by ~40 kJ per mole of Ni atoms at the smallest sizes measured). Due to the much slower diffusion of Ni atoms at 100 K, they are not able to nucleate particles at step edges, but at 300 K they can. When the particle diameter exceeds ~1.3 to 1.5 nm, the heat of Ni adsorption under all three conditions (i.e., $CeO_{1.95}$(111) at 300 K, $CeO_{1.8}$(111) at 300 K, $CeO_{1.95}$(111) at 100 K) only show small differences between each other. Apparently, the new Ni atoms that add to particles larger than ~1.4 nm predominantly bind to sites that are far enough from step edges that they feel little effect of the step sites. Because of the much larger particle number density at 100 K than at 300 K, this particle size (> 1.4 nm) is not reached until a 4-fold higher coverage at 100 K. This size difference explains why the heats of adsorption in Fig. 2 at 100 K remain below those at 300 K until very high coverage.

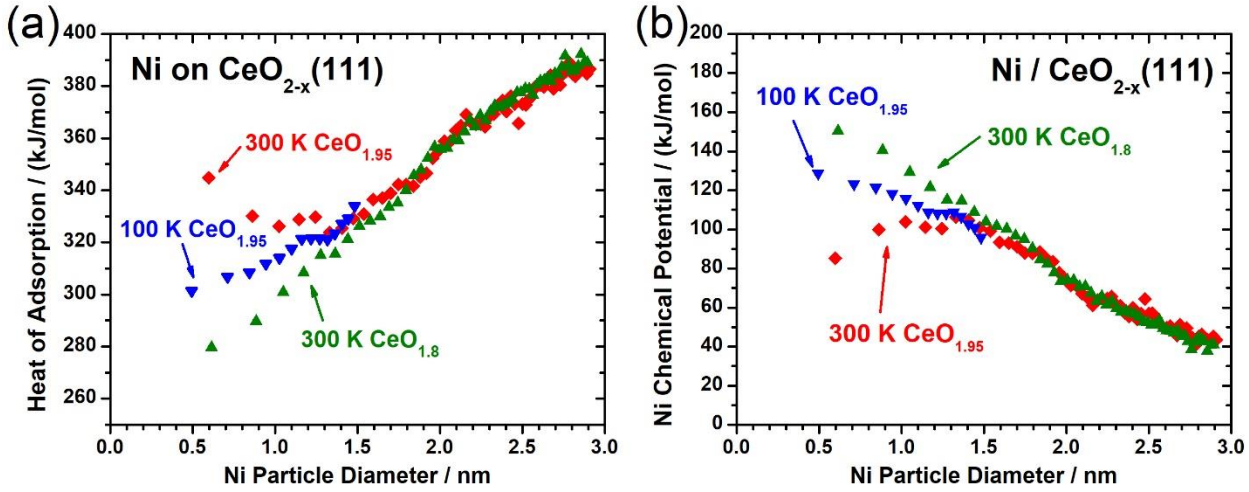

Figure 3. (a) Differential heat of Ni adsorption on CeO_{2-x}(111) at 300 and 100 K as a function of Ni average particle (flat-disk) diameter to which Ni atoms add. (b) Chemical potential of Ni atoms in Ni particles versus the average Ni particle diameter on CeO_{2-x}(111) at 300 and 100 K. Red diamonds, green triangles and blue triangles correspond to $CeO_{1.95}$ at 300 K, $CeO_{1.8}$ at 300 K, and $CeO_{1.95}$ at 100 K respectively.

As reported previously,[60] we can convert the differential heats of Ni adsorption measured here to the chemical potential of Ni atoms by assuming that the entropic contribution to the free energy is negligible compared to the huge enthalpic differences measured here. The difference between the chemical potential of Ni atoms in nanoparticles with a given diameter D and the chemical potential of Ni atoms in bulk Ni metal (set as the zero reference of chemical potential) equals the sublimation heat of bulk Ni minus the heat of Ni adsorption onto Ni nanoparticles with diameter D.[60] The data in Figure 3a have been replotted in Figure 3b as the chemical potential of Ni atoms in Ni nanoparticles versus the average particle diameter. As seen, the chemical potential generally decreases with increasing particle size, as has been reported for many related systems, and is largely related to the increasing number of metal-metal bonds per atom with increasing size.[26-28, 60] The chemical potential initially increases with increasing particle size for $CeO_{1.95}$(111) at 300 K, due to the initial population of more stable sites at step edges, which saturate quickly as coverage increases.

It appears from Figure 3 that Ni particles do not nucleate at step edges on the $CeO_{1.8}$(111) surface even at 300 K, or that step edges do not bind Ni significantly more strongly than terraces on this heavily reduced ceria surface, especially since O vacancies prefer to form at step edges, as noted above.

3.4. Charge Transfer from Ni to CeO_{2-x}(111) during Deposition

The change of Ce oxidation state in the CeO_{2-x}(111) surface during Ni deposition was monitored by monitoring the change in the Ce 3d XPS peak lineshape. The percentage of Ce^{3+} in the Ce 3d XPS probe depth (~1 nm) was determined from lineshape fitting of the XPS Ce 3d peak as described previously.[26, 61] The Ce^{3+} percentage is plotted with respect to Ni coverage in Figure 4. The Ce^{3+} percentage increases rapidly with the Ni coverage up to 2 ML for $CeO_{1.95}$(111) at 300 and 100 K. Above 2 ML, the Ce^{3+} percentage does not change much with the Ni coverage, remaining very near the high-coverage (10 ML) limit of 22% at 300 K and 19% at 100 K. For $CeO_{1.8}$(111), the Ce^{3+} percentage also increases in the first 2 ML, but only from 41% to 46%, and again stays fairly constant with coverage above 2 ML.

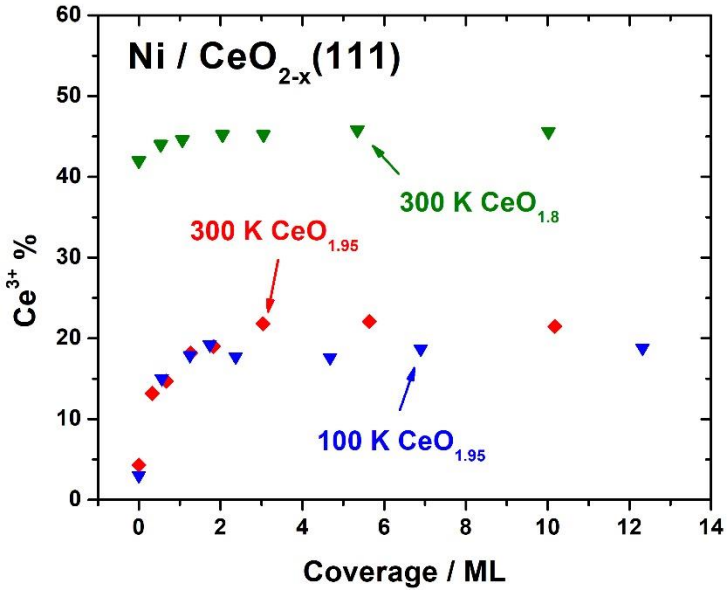

Figure 4. Percentage of Ce^{3+} (with the rest as Ce^{4+}) in the XPS probe depth versus Ni coverage based on lineshape fitting of the XPS Ce 3d peak measured during Ni deposition on $CeO_{1.95}$(111) at 300 K (red), $CeO_{1.8}$(111) at 300 K (green) and $CeO_{1.95}$(111) at 100 K (blue).

To quantify the extent of charge transfer per Ni atom to the film, we assume that the Ce atoms in the CeO_{2-x}(111) film are reduced by the electrons donated from the Ni atoms by the percentage plotted in Figure 4, but only down to the XPS probe depth of 1.0 nm, with no reduction below that. (Using the TPP-2M equation[62] to calculate, the electron inelastic mean free path in CeO_2 for Ce 3d XPS peak is 1.24 nm. Since the XPS data was taken with the energy analyzer at 45˚ to the normal angle of the sample, 70% of the XPS signal of Ce 3d peak comes from the first 1.0-nm-thick layer of ceria in the sample.) Using the number of Ce atoms per unit area in this

probe depth (2.5×10^{15} Ce atoms per cm^2), the data point in Figure 4 at each Ni coverage can then be converted to the average number of electrons donated per Ni atom, as done previously for Cu on this same surface.[26] If we further assume that Ni can only be in the form of neutral Ni or Ni^{2+}, this average number of electrons donated per Ni atom can be converted to the fraction of total Ni that is oxidized to Ni^{2+}. Figure 5a shows the resulting number of electrons donated per Ni atom and fraction of Ni^{2+}, calculated based on data in Figure 4, plotted versus Ni coverage. These both decrease rapidly with coverage, and are much smaller values on the more reduced ceria.

We observed that the Ni $2p_{3/2}$ XPS peak's binding energy (BE) at low Ni coverages had large contributions in the region expected for Ni^{2+}. This was studied in more detail by Carrasco et al.[6], as shown in Figure 5b, where their Ni $2p_{3/2}$ BE for Ni on $CeO_2(111)$ at 300 K is plotted as a function of Ni coverage. For a coverage of 0.15 ML of Ni, they reported a shift of ~2 eV with respect to the reported value for metallic Ni, which indicates the formation of Ni^{2+}.[63] Zhou et al.[64] also observed with XPS that when ~0.5 ML Ni (which is ~1.2 ML in the definition of this paper) is deposited onto the fully oxidized $CeO_2(111)$ at 300 K, about 25% of the total Ni is oxidized to Ni^{2+}.

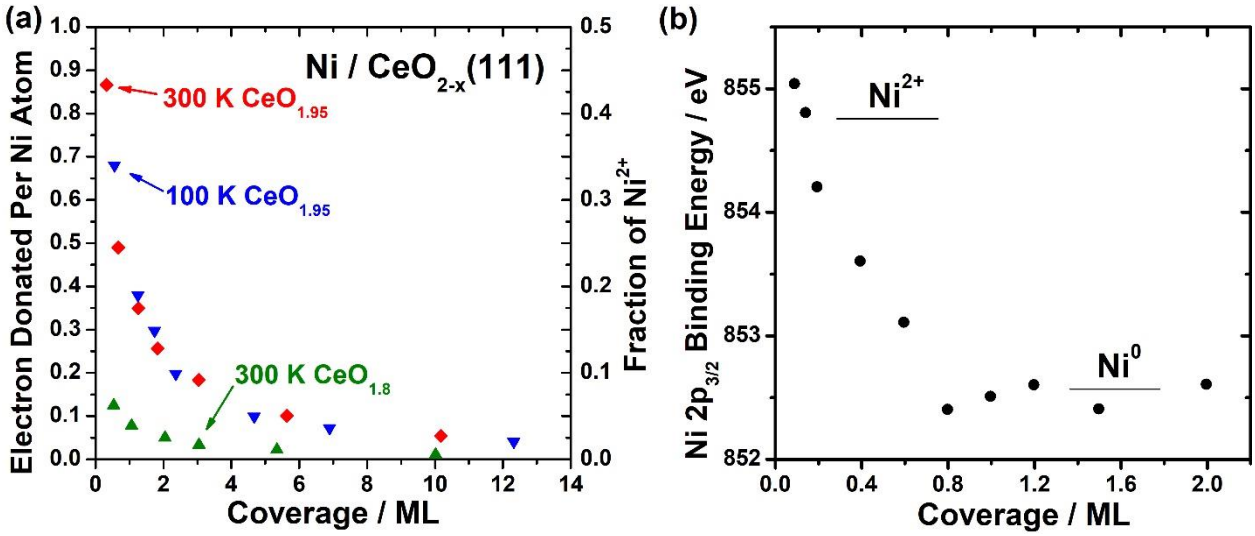

Figure 5. (a) Average number of electrons donated to ceria per Ni atom and corresponding fraction of total Ni that is oxidized (assuming it is Ni^{2+}) plotted as a function of Ni coverage; (b) Variation of the Ni $2p_{3/2}$ XPS binding energy as a function of Ni coverage on $CeO_2(111)$ at 300 K as was reported in the Supplementary Information of ref.[6]

For the convenience of comparison to DFT calculations, the number of electrons donated per Ni atom and the fraction of Ni^{2+} are also replotted as a function of the average number of Ni atoms per Ni nanoparticle in Figure 6. Here, one clearly sees that the fraction of Ni^{2+} is larger for a given particle size when grown at 300 K (where they nucleate at steps and have a higher heat of adsorption) than at 100 K where they nucleate at terraces and are less stable. Thus, step edges seem to be important in making the Ni^{2+} species stable. Alternatively, the temperature could have a direct effect in that the process to make Ni^{2+} might have some activation barrier that is not reached at 100 K.

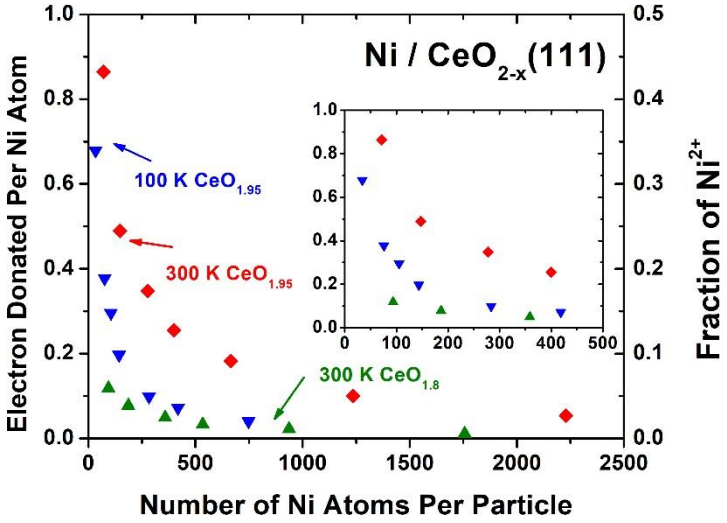

Figure 6. Average number of electrons donated to ceria per Ni atom and corresponding fraction of total Ni that is oxidized (assuming it is Ni^{2+}) from Figure 5a replotted as a function of number of Ni atoms per particle.

3.5. DFT Models

The $Ni_n/CeO_2(111)$ (n=1-7, 9, 13, 19, 24, 26, 29 and 32) surfaces were modeled with DFT by supercells with (3×3) surface periodicity, see Figure 7, with calculated ceria bulk equilibrium lattice constant (CeO_2: 5.485 Å, DFT+U). A CeO_2 slab of six atomics layers, i.e., two O-Ce-O trilayers, separated by at least 13 Å-thick vacuum layer, was used as model of the ceria support. Monkhorst-Pack[65] grids with (2×2×1) k-point sampling were used. All atoms in the three bottom atomic layers were fixed at their optimized bulk-truncated positions during geometry optimization, whereas the rest of the atoms were allowed to fully relax. The structures of the ceria-supported Ni_1, Ni_2, Ni_4.flat, and Ni_4.pyr aggregates (Figure 7) correspond to the ones previously reported,[2, 11, 14, 16] for which the locations of the Ce^{3+} ions, resulting from the metal-support interaction, were

optimized. For the other Ni aggregates considered, some different adsorption sites were explored, but different Ce^{3+} configurations were not. Note that for Ni_n (n > 19), the (3×3) surface unit cell is not large enough to isolate the Ni_n aggregates, and the models correspond to continuous rows of supported Ni atoms, i.e., infinitely long 1D islands (i.e., stripes or wires) of Ni that are several Ni atoms wide. Selected calculations were performed for some $Ni_n/CeO_2(111)$ systems with (4×4), (2×2) and (1×1) surface periodicity and (1×1×1), (3×3×1), and (6×6×1) k-point sampling, respectively, in order to evaluate possible variations in the number of electrons transferred from the Ni_n aggregates to the ceria support as a function of Ni loading.

Reduced extended $CeO_{2-x}(111)$ surfaces were modeled with different concentrations of oxygen vacancies (Θ_{Ovac}=1/4, 1/2, and 3/4; Θ_{Ovac} = Nv/N, where Nv and N are the number of surface plus subsurface vacancies in the reduced overlayer and the total number of oxygen atoms in a single non-reduced oxygen atomic layer of the same cell, respectively) using a slab of nine atomic layers with (2×2) periodicity, as employed in previous work.[11] Furthermore, one and two layers of Ce_2O_3 on $CeO_2(111)$ as well as the fully reduced (A-type) $Ce_2O_3(0001)$ surface (Ce_2O_3: a_0/c_0 = 3.92/6.18 Å and internal parameters u_{Ce}/u_O = 0.2471/0.6448, ferromagnetic state, DFT+U) were also modeled; only the interaction of Ni_1 species on the reduced supports were considered, and this was done without accounting for long-range dispersion corrections.

The oxidation state of a given Ce ion (Ce^{4+} or Ce^{3+}) was determined by considering its local magnetic moment (the difference between up and down spins on the ion), which can be estimated by integrating the site- and angular momentum-projected spin-resolved density of states over spheres with radii chosen as the Wigner−Seitz radii of the PAW potentials. The magnetic moment of the Ce^{4+} ($4f^0$) and Ce^{3+} ($4f^1$) ions is 0 and ~1 μ_B, respectively, because the occupation of the Ce *f* states is 0 and ~1, respectively. As for the oxidation state of the Ni atoms in the supported clusters, using the Bader analysis method,[66] we obtained that only those Ni atoms in direct bonds to the ceria support are partially oxidized, and thus, the average oxidation state of these atoms is calculated as the total number of electrons transferred to the ceria support divided by the number of Ni atoms with direct bonds to the support (Figure 7).

The integral heat of adsorption of Ni gas atoms forming Ni_n clusters on the $CeO_2(111)$ support was calculated at 0 K as E_{ads}= −1/n [$E(Ni_n/CeO_2)$ – $E(CeO_2)$ – n*$E(Ni_{atom})$] where $E(Ni_n/CeO_2)$ and $E(CeO_2)$ are the total energies of the $Ni_n/CeO_2(111)$ and $CeO_2(111)$ surfaces, and

$E(Ni_{atom})$ is that of a gas-phase Ni^0 atom in the d^9s^1 configuration, calculated with a (12×11×16) $Å^3$ periodic cell and the Γ-point. The lattice parameter of bulk fcc Ni was optimized (Ni_{bulk}: 3.48 Å, DFT+D3), using a Monkhorst-Pack grid with (15×15×15) k-point sampling of the Brillouin zone, and the heat (enthalpy) of sublimation of bulk Ni (bulk cohesive energy) was calculated to be $\Delta H^{calc}_{sub,Ni}$ = 518 kJ/mol. These are in good agreement with prior results.[67, 68]

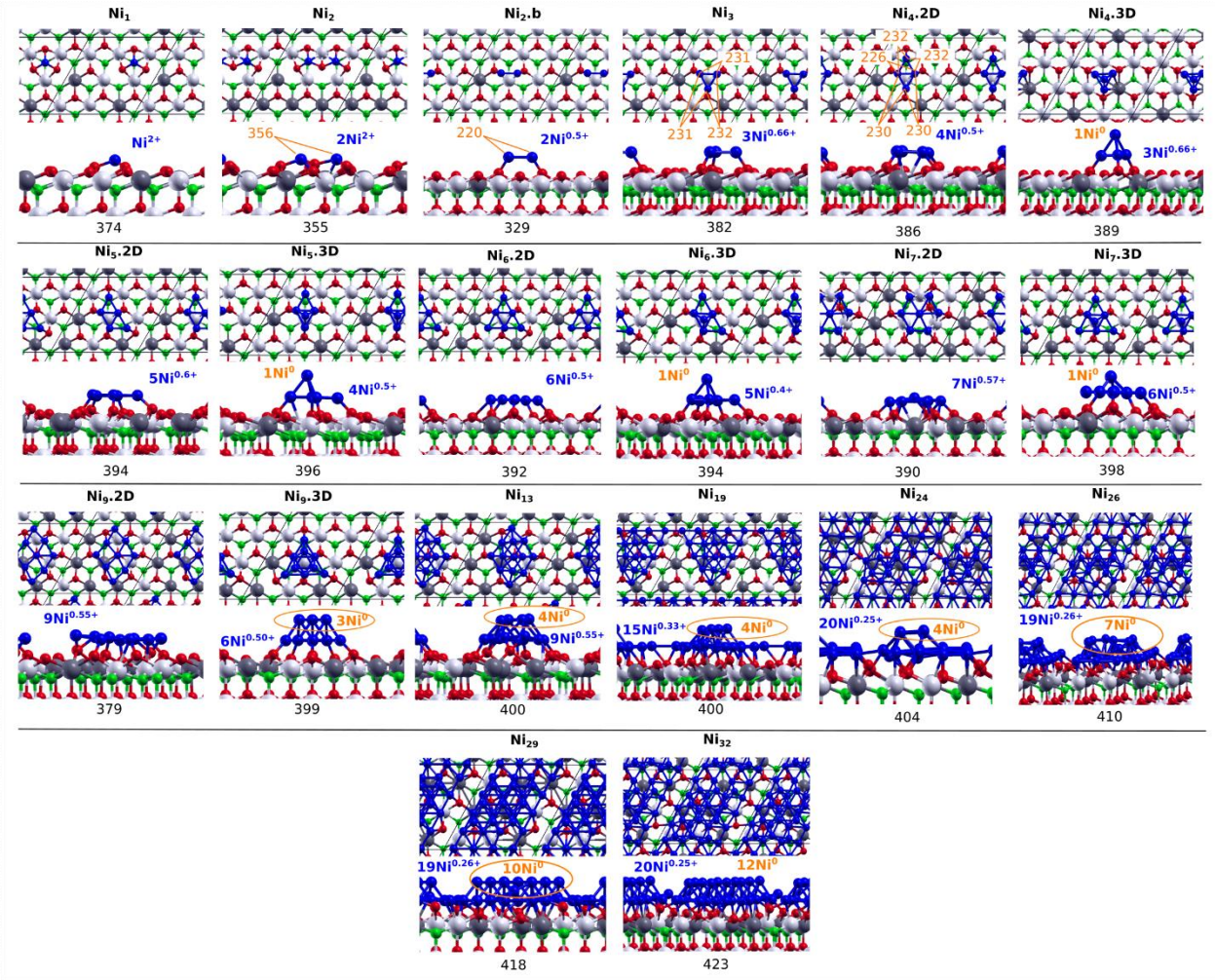

Figure 7: Models of $Ni_n/CeO_2(111)$ (n=1-7, 9, 13, 19, 24, 26, 29 and 32). Surface/subsurface oxygen atoms in the outermost O–Ce–O trilayer are depicted in red/green, Ce^{4+} in white, and Ce^{3+} in gray. Values of the integral heat of adsorption of Ni_n species are listed below each structure, in kJ/mol per Ni atom (relative to Ni gas). Optimized Ni-Ni bond lengths in pm for Ni_2, Ni_3 and Ni_4.2D are indicated in orange.

We modeled stoichiometric <110>-type steps by adding a continuous stripe (or wire) of CeO_2 that was three atomic layers thick and covered 3/5 of the surface on top of a six-layer-thick (5×3) $CeO_2(111)$ slab (like described above) and (1×2×1) k-point sampling. This is similar to

methods that have been used preciously to model steps of CeO_2(111) using DFT.[59, 69] Reduced <110>-type steps with varying fractions of missing step-edge oxygen atoms ($\Theta_{Ovac,step}$=1/3, 2/3, and 1) were also modeled. This added "CeO_2 wire" had stoichiometry Ce_9O_{18} per (5×3) unit cell when not reduced, decreasing to Ce_9O_{15} for the most fully reduced step edge. The adsorption of Ni_1 species on these stoichiometric and reduced step edges were studied. The locations of the Ce^{3+} ions, resulting from the removal of the step-edge oxygen atoms and from the Ni-ceria interactions, were not optimized in detail when modelling step sites.

3.6. Ni monomers on CeO_2 and CeO_{2-x}(111) terraces: DFT results

On CeO_2(111), an isolated Ni_1 species was found to adsorb on a hollow site coordinated to three surface oxygen atoms with E_{ads} = 374 kJ/mol, in line with previous studies (Figure 7).[2, 11] As a result of strong metal-support interactions between Ni_1 and CeO_2, two electrons from Ni are transferred to the support, generating two Ce^{3+} ions, and the Ni atom becomes oxidized to Ni^{2+} (d^8). This is qualitatively consistent with the experimental observations in Figure 5, although the extent of charge transfer is not as large experimentally. This is probably related to the fact that the experimental surface is not stoichiometric CeO_2, but instead is already partially reduced to $CeO_{1.95}$, and the extent of charge transfer decreases with the degree of reduction (see above). For Cu adsorption on CeO_{2-x}(111), we also found that such small amounts of pre-reduction (2.5%) greatly decreased the extent of charge transfer at the lowest Cu coverages compared to stoichiometric CeO_2.[26]

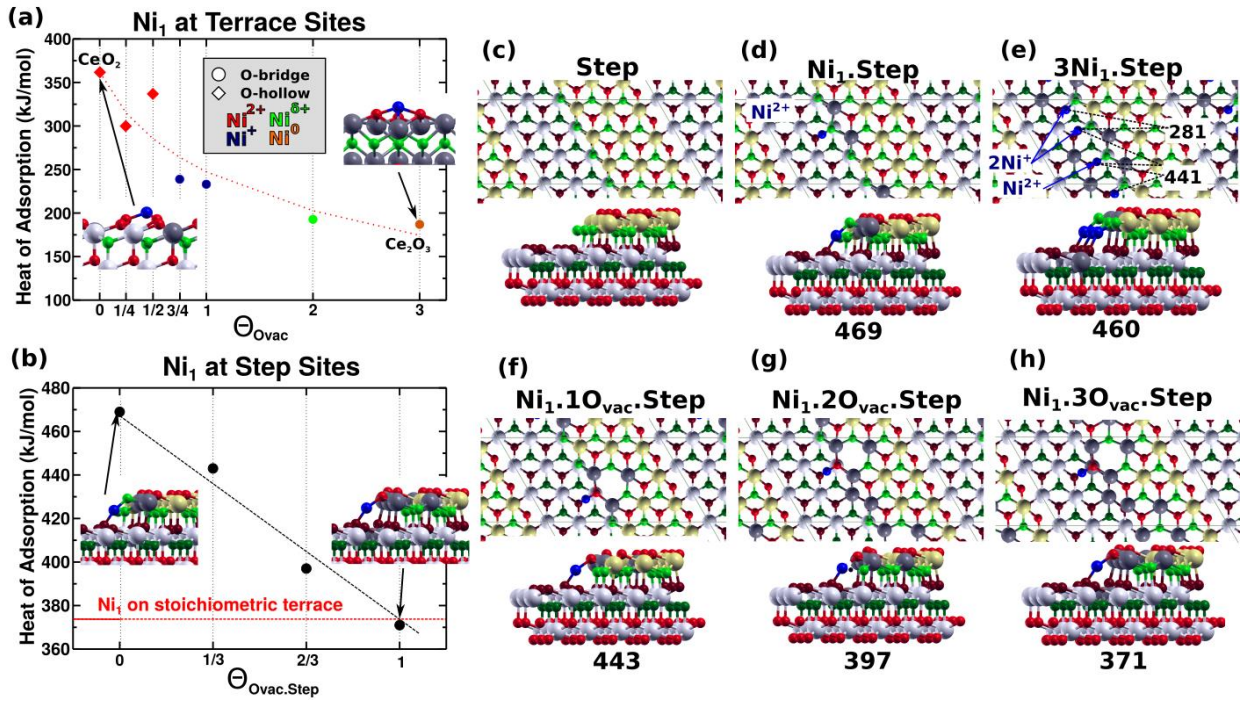

Figure 8: (a) Calculated heat of adsorption of a single Ni atom on the CeO_2(111) surface, CeO_{2-x}(111) with different concentrations of subsurface oxygen vacancies (Θ=1/4, 1/2, and 3/4, see text). Also shown are results for 1 and 2 layers of Ce_2O_3 on CeO_2(111) and a slab of pure Ce_2O_3(0001), plotted at $\Theta_{Ovac,step}$= 1, 2 and 3, respectively. The Ni oxidation state is color coded as shown ($0 < \delta < 1$), and the adsorption site corresponds to the most stable one. Note that the slab model and method used in these calculations slightly differ from those used to obtain the values reported in Figure 7 (see text), explaining the difference of 11 kJ/mol in the heat of adsorption of a single Ni atom on the CeO_2(111) surface. (b) Calculated heat of adsorption of Ni monomer at a <110>-type step as a function of the step-edge O vacancy fraction ($\Theta_{Ovac,step}$= 0, 1/3, 2/3, and 1). The red dotted line corresponds to the heat of adsorption of one Ni atom on the stoichiometric terrace (374 kJ/mol, Figure 7). Atomic structures of the (c) stoichiometric <110>-type steps with (d) one and (e) three Ni atoms and of the (f)-(h) reduced steps with one Ni atom. Values of the heat of adsorption of Ni species are listed below each structure, in kJ/mol per Ni atom (relative to Ni_1 gas).

Figure 8a shows the calculated heat of adsorption of a nickel atom on reduced CeO_{2-x}(111) surfaces. The two excess electrons resulting from the creation of a (neutral) oxygen vacancy have been reported to be localized at cation sites in the outermost plane of cations, but not adjacent to the vacancies, driving the $Ce^{4+} \rightarrow Ce^{3+}$ reduction; and, the energetically most stable near-surface oxygen vacancy structures for a broad range of vacancy concentrations all have their vacancies at subsurface oxygen sites.[70-73] As the degree of near-surface reduction increases, the adsorption energy of the Ni atom decreases and at the same time, Ni adatoms recover their metallic character

($Ni^{2+} \rightarrow Ni^{1+} \rightarrow Ni^{0}$). In other words, as the concentration of Ce^{3+} ions increases, it gradually becomes more and more difficult for Ni to transfer electrons to the already reduced support, as observed experimentally (Figure 6). The results in Figure 8 also help explain the experimental observations that the binding of Ni at low coverage is stronger on a ceria surface which is less reduced (cf. Figures 2 and 3a). This suggests that the ability of ceria to stabilize oxidized nickel species (Ni^{2+}) on the CeO_2 surface, by re-localizing electrons on localized *f*-states (Ce^{3+}), is a key factor in determining the Ni heat of adsorption.

3.7. Ni monomers at CeO_2(111) and CeO_{2-x}(111) step sites: DFT results

Comparison of the heats of adsorption of Ni monomers on the flat stoichiometric CeO_2(111) terraces (374 kJ/mol, Figure 7) and at stoichiometric <110> step edges (Figure 8c) shows that the step edge binds Ni_1 more strongly by 95 kJ/mol (Figure 8d). In both sites, the Ni binds as Ni_1^{2+}. These calculations thus predict that decoration of the stoichiometric step with Ni species will occur before adsorption on the terraces. The heat of adsorption of three Ni_1 species (Figure 8e), which corresponds to the maximum possible coverage of monodispersed Ni_1 species at the step edge, is almost the same as a single Ni_1, still also ~90 kJ/mol per Ni atom more strongly bound to the step edge than isolated Ni_1 species on the flat terrace. This is consistent with the observed minimum in the heat of Ni adsorption versus coverage on the $CeO_{1.95}$(111) surface at 300 K (Figure 2), which we attributed to the existence of stronger-binding defect (step-edge) sites that are occupied first, i.e., at low Ni coverage.

However, on the more reduced $CeO_{1.8}$(111) surface, no minimum in the calorimetric heat of Ni adsorption versus coverage has been observed, and the measured heat is always lower than on the nearly stoichiometric surface (Figure 3a). This is consistent with the calculated heat of adsorption of Ni at the step as a function of the step-edge oxygen vacancy fraction ($\Theta_{Ovac,step}$, Figure 8b), which shows that as the number of available step-edge oxygen atoms decreases, step sites eventually become less stable than terrace sites when all the step-edge oxygen atoms are removed.

We also calculated the average step-edge oxygen vacancy formation energy as a function of the step-edge O vacancy fraction ($\Theta_{Ovac,step}$) and found that oxygen atoms at the step are always

easier to remove than those at the terrace. The average defect formation energy was 169, 207 and 219 kJ/mol for $\Theta_{Ovac,step}$=1/3, 2/3, and 1, respectively, and 265 kJ/mol at a terrace site, calculated using the model in Figure 8c without optimizing the location of the excess charge. This validates our claim above (based on prior literature) that the O vacancies are mainly at the step edges, which also suggests that on the more reduced $CeO_{1.8}$(111) surface studied experimentally here, there may be no O atoms on the step edges.

3.8. Ni clusters on stoichiometric CeO_2(111) terraces: Heat of adsorption and charge transfer by DFT

The formation of Ni_2 dimeric structures was considered, as studied in previous work.[16] In the case of two Ni atoms at neighboring hollow sites separated by 3.56 Å (Figure 7), each Ni atom transfers two electrons to the ceria support, generating four Ce^{3+} ions and two Ni^{2+} species. The adsorption energy of such a Ni pair is E_{ads}= 355 kJ/mol (per Ni atom, relative to Ni gas). Therefore, bringing two Ni^{2+} species closer but without forming a Ni-Ni bond destabilizes the system by 38 kJ/mol [2×Eads(Ni_2) -2×Eads(Ni_1)], which implies a repulsive interaction of 38 kJ/mol between the positively charged Ni^{2+} atoms at this separation. We addressed whether a Ni_2 dimeric structure forming a Ni–Ni bond ($Ni_{2.}b$) is energetically preferred over two well-separated Ni_1^{2+} species by adsorbing such a $Ni_{2.b}$ species which have an optimized Ni–Ni bond length of 2.20 Å (cf. Figure 7). This results in one Ce^{3+} ion, and thus two partially oxidized $Ni^{0.5+}$ atoms. The adsorption energy of the $Ni_{2.}b$ dimer is only E_{ads}= 329 kJ/mol, i.e., the system is 90 kJ/mol *less* stable than two isolated Ni_1^{2+} species. Even though the Ni atoms in the $Ni_{2.b}$ dimer have a low charge, it is still too high to allow intrinsic Ni-Ni bonding that exceeds the $Ni^{0.5+}$-$Ni^{0.5+}$ charge repulsion. This repulsive interaction of the two ceria-supported $Ni^{0.5+}$ species of 90 kJ/mol for the $Ni_{2.}b/CeO_2$(111) system (cf. Figure 7) is 68 kJ/mol lower than the simple Coulomb repulsion of two +0.5 point charges at the same separation (2.20 Å) in vacuum (158 kJ/mol). The difference reflects some type of attractive bonding between the two Ni cations that partially overcomes the Coulomb repulsion.

In the case of a Ni_3 cluster, the Ni atoms form a flat triangle with three nearly equal Ni–Ni bonds of length 2.31-2.32 Å (Figure 7), two Ce^{3+} ions are formed, and therefore each of the three Ni atoms has a charge of +0.67. The adsorption energy of the Ni_3 trimer is E_{ads}= 382 kJ/mol; hence,

compared to three isolated Ni_1^{2+} species, the Ni_3 cluster is 24 kJ/mol more stable (or 8 kJ/mol per Ni atom).

As for Ni_4, both three dimensional clusters with pyramidal shape (Ni_4.3D) and bi-dimensional flat rhombohedral-shaped (Ni_4.2D) clusters were considered, as studied previously.[2] The stability of these clusters is comparable, namely, E_{ads}= 389 and 386 kJ/mol for Ni_4.3D and Ni_4.2D, respectively (Figure 7). These Ni_4 species also reduce the ceria support upon adsorption, with the formation of two Ce^{3+} ions. In the Ni_4.3D case, these two electrons are transferred from the three Ni atoms forming the pyramid base, which are partially oxidized, $3\times Ni^{0.66+}$, whereas the top Ni atom remains as Ni^0. In the Ni_4.flat, all four Ni atoms in direct contact with the support are oxidized, $4\times Ni^{0.5+}$. As with the Ni atoms in the Ni_3 cluster, those in the Ni_4 clusters do not repel each other. For instance, the Ni_4.2D structure ($4\times Ni^{0.5+}$) is more stable by 228 kJ/mol [$4\times E_{ads}(Ni_4.2D) - 4\times E_{ads}(Ni_{2.}b)$] than two isolated Ni_2.b dimers ($2\times Ni^{0.5+}$ each). Even if the Ni atoms in the Ni_4.2D and Ni_2.b structures have a similar charge (+0.5), the larger number of Ni–Ni bonds in the Ni_4.flat cluster, with one bond length of 2.26 Å and four average bond lengths of 2.31 Å, is what optimally stabilizes the structure.

As the number of Ni atoms in the nanoparticles increases beyond three, the formation of 3D structures is preferred over flat ones (cf. Figure 7), in agreement with the experimental observation that Ni grows as 3D particles. For instance, the energy gained by adding one Ni atom to the flat Ni_4.2D cluster [$5\times Eads(Ni_5) - 4\times Eads(Ni_4.2D)$] is by 10 kJ/mol larger if a Ni_5.3D structure is formed (436 kJ/mol) (Figure 7), as compared to a 2D Ni_5 aggregate (426 kJ/mol). The configuration of the Ni_5, Ni_6 and Ni_7 nanoparticles corresponds to 3D structures with 4, 5 and 6 Ni atoms, respectively, in contact with the ceria support, with $2\times Ce^{3+}$ ions for the Ni_5, Ni_6 structures and $3\times Ce^{3+}$ ions for the Ni_7 one. As for the case of Ni_4, electrons are transferred only from the Ni atoms in direct contact with atoms of the ceria support, and these are partially oxidized ($4\times Ni^{0.5+}$, $5\times Ni^{0.4+}$ and $6\times Ni^{0.5+}$ for the Ni_5, Ni_6 and Ni_7 nanoparticles, respectively), whereas the Ni atoms on top (not in direct contact to the ceria) remain as Ni^0. Also, for the Ni_9 ($3\times Ce^{3+}$), Ni_{13} ($5\times Ce^{3+}$) and Ni_{19} ($5\times Ce^{3+}$) aggregates, only the six, nine and fifteen Ni atoms, respectively, in direct contact with the oxide support are partially oxidized ($6\times Ni^{0.50+}$, $9\times Ni^{0.56+}$ and $5\times Ni^{0.34+}$, respectively), whereas the Ni atoms on top of the oxidized nickel retain their metallic character (Ni^0). Finally, the continuous stripes of Ni that we considered (i.e., Ni_{24}, Ni_{26}, Ni_{29} and Ni_{32}) donate 4 electrons

for Ni_{24} and Ni_{32} and 5 electrons for Ni_{26} and Ni_{29} to the support ($5\times Ce^{3+}$). In the Ni_{24}, Ni_{26}, Ni_{29} and Ni_{32} stripes, also only the atoms in direct contact with the ceria support are partially oxidized (cf. Figure 7).

In summary, the DFT results produce firm computational evidence that for low Ni loadings on the $CeO_2(111)$ surface, for which a large dispersion of small Ni nanoparticles is observed,[1,64] the ceria support induces strong electronic perturbations in chemisorbed Ni species which are directly at the Ni-ceria interface, whereas there is a rapid weakening of the Ni-ceria interactions with increasing Ni loading, for which 3D nanoparticles form.[1,64]

4. Discussion

Figure 9 compares the calculated integral heat of adsorption for the thermodynamically stable $Ni_n/CeO_2(111)$ systems with those obtained experimentally (cf. Figure 2), where the calculated points have been shifted by −88 kJ/mol [$\Delta H^{calc}_{sub,Ni}\left(518\frac{kJ}{mol}\right) - \Delta H^{exp}_{sub.Ni}(430\frac{kJ}{mol})$]. This correction corresponds to the 88 kJ/mol difference between the calculated bulk cohesive energy (sublimation energy) of bulk Ni(solid) with the PBE exchange-correlation functional with long-range dispersion corrections (DFT-D3), as compared to the experimental value.

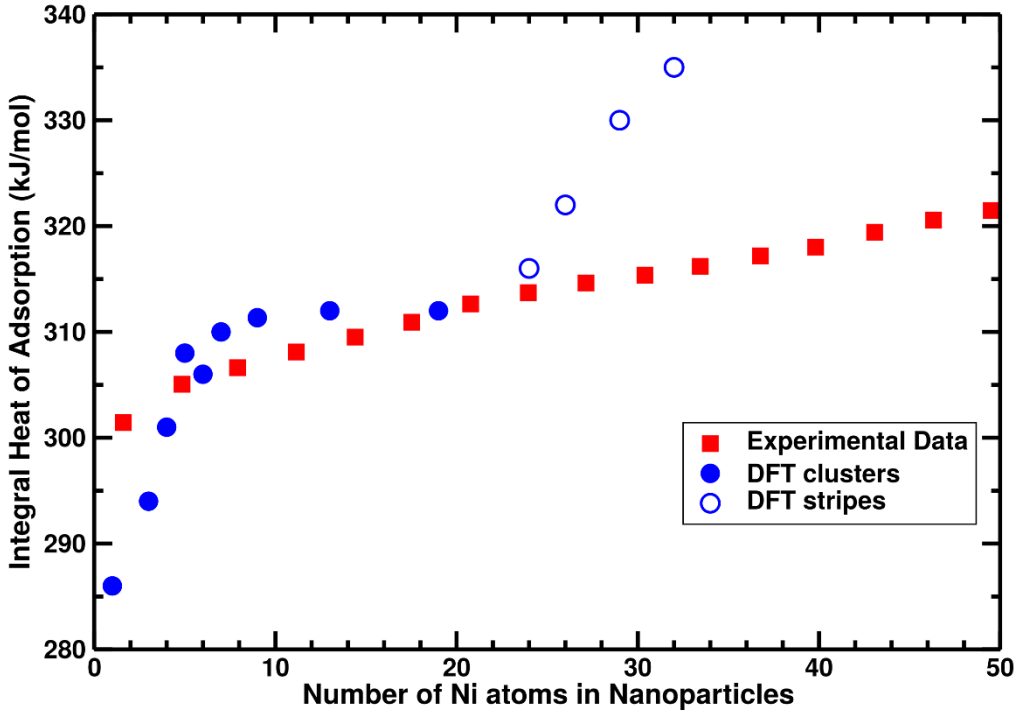

Figure 9: Integral heat of adsorption as function of the number of Ni atoms in the Ni_n aggregates. Experimental data for adsorption at 100 K (where terrace sites are predominantly populated) (red squares), calculated DFT data (blue filled and empty circles). For n > 19, the Ni_n aggregates in DFT correspond to continuous Ni stripes or wires (blue empty circles). The DFT points were shifted by 88 kJ/mol to smaller values (see text).

The experimentally determined heats of adsorption are larger than the DFT ones for 1 and 3 atom clusters by 15 and 10 kJ/mol, respectively, after this 88 kJ/mol correction in Figure 9). This may be due to the fact that the cluster sizes could have been underestimated in the first two pulses in the heat measurements of Figures. 2, 3 and 9. Although the LEIS measurements of Figure 1 are consistent with a constant number density of Ni clusters, independent of coverage, those measurements did not extend down to such low coverages as the heat measurements, so it is possible that in the first two heat points, the Ni clusters had not yet reached their saturation density, as we assumed here in estimating cluster sizes. For higher Ni loading, the DFT heats plotted in Figure 9 are larger than the experimental ones. This is actually to be expected based on the wire-like nature of the Ni aggregates modelled by DFT, which have more Ni–Ni bonds per Ni atom than in the corresponding isolated clusters studied experimentally.

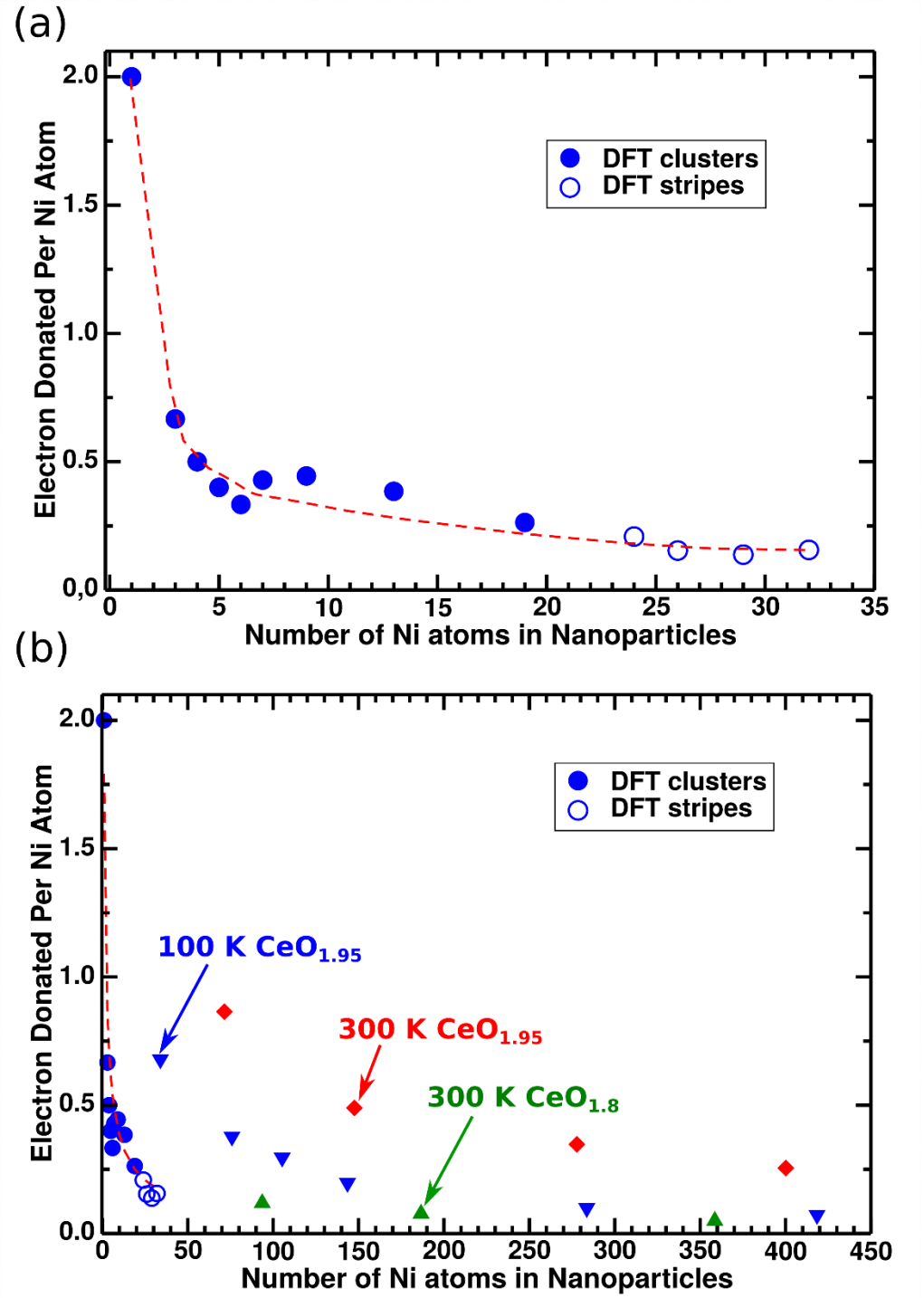

Figure 10: (a) Calculated number of electrons donated per Ni atom as a function of the number of Ni atoms in the nanoparticle. (b) DFT data from part (a) replotted over a larger range for comparison to the experimental data from Figure 6.

The comparison and the discussion above reveal that, due to the strong Ni-ceria support interaction and its large charge transfer, at least three Ni atoms are required to make Ni clusters stable. Only then can the intrinsic Ni-Ni bond energies help win out over repulsive interactions between partially charged Ni atoms at the Ni-ceria interface.

Figure 10a shows the number of electrons transferred per Ni atom versus cluster size as calculated by DFT. The extent of charge transfer per Ni atom clearly decreases rapidly with cluster size, but for a given size we found it to be generally independent of the size of the unit cell, as discussed below. Figure 10b compares this number of electrons transferred per Ni atom versus particle size as calculated with the experimental results reported in Figures 5a and 6.

As seen in Figure 10b, the charge transferred per Ni atom decreases strongly with particle size in all three curves. However, it decreases much more rapidly in the DFT calculations than in the closest corresponding experiment (i.e., $CeO_{1.95}$(111) at 100 K, where the particles are at terrace sites like in the DFT). The transferred charge in the experiments also decreases with size much more rapidly at 100 K than at 300 K, so that the charge transferred per Ni atom on $CeO_{1.95}$(111) is 3- to 4-fold larger for the same particle size at 300 K than at 100 K. This may be related to the fact that the clusters are at step edges at 300 K but on terraces at 100 K, although this is surprising since the 2.5% O vacancies in this $CeO_{1.95}$(111) surface concentrate at step edges, and O vacancies clearly decrease the extent of charge transfer (see above). However, step edges may have other electronic or structural characteristics that enhance charge transfer in spite of these extra O vacancies. For example, charge-transfer-induced lattice strain is probably relieved more easily near steps. (Earlier DFT calculations have shown that such charge transferred to CeO_2(111) and the corresponding conversion of Ce^{4+} to Ce^{3+} leads to lattice expansion parallel to the surface.[74]) Given that the DFT calculations are at 0 K, the three curves in Figure 10b separate by temperature, with greater charger transfer at higher temperature. Temperature seems unlikely to be the intrinsic reason for this, since the only reasonable explanation would be some activation energy associated with charge transfer of a type that we have never seen reported.

For the same particle size in Figure 10b, the total Ni coverages are quite different for the three curves for CeO_2(111) and $CeO_{1.95}$(111), since the Ni clusters are much closer together in the DFT models than in the experiments at 100 K, and they are closer together in the experiments at 100 K than at 300 K. It is possible that there are strong dipole-dipole repulsions between clusters,

since the clusters carry so much charge and have their counter charge in the outermost ceria plane at the metal-ceria interface according to the DFT results. These repulsions get stronger as the distance between parallel dipoles decreases, and are therefore well known to lead to depolarization of adsorbate-substrate bonds as their coverage increases.[75] So these different coverages would affect charge transfer in the way seen here: higher coverages lead to less charge transfer for the same cluster size. The data for these curves in Figure 10b are replotted versus coverage in Figure 11. When plotted in this way, all three data sets converge into a single curve, which lends support to the proposal that the differences in Figure 10b are largely associated with this effect of coverage (cluster separation) on dipole-dipole repulsions between clusters. We tested this effect directly with DFT by changing the unit cell size for the same cluster size and shape. For one Ni atom with (4×4), (3×3), (2×2) periodicity, DFT shows that two electrons are transferred to the ceria support (Ni^{2+}), whereas for the (1×1) unit cell, only 2/3 of electron is transferred ($Ni^{0.66+}$). However, for both the Ni_3 and Ni_4.3D clusters with (3×3) and (2×2) periodicity, two electrons are transferred independent of the size of the unit cell ($3\times Ni^{0.67+}$). This can be seen as the pairs of DFT points in Figure 11 with nearly the same charge transfer but quite different coverages (cf. Ni_5.3D and Ni_{13} with about 0.4 electrons donated per Ni atom but corresponding to 0.56 and 1.45 ML). This gives rise to the greatest deviations from the single curve fit through these data in Figure 11. Since these DFT calculations do not show a direct effect of coverage on charge transfer, we cannot be sure that the nice correlation with coverage in Figure 11 that seems to bring all three data sets into pretty close agreement is really due to the direct effect of coverage (i.e., cluster separation). It may be that the largest unit cell size in the DFT calculations is still not large enough to see this effect, since the cluster density used in the DFT models is much higher than in the experiments. An alternative explanation is that the charge transfer in the 300 K experiments is greater for the same

cluster size than in the 100 K experiments due to the fact that the clusters are at step edges at 300 K but on terraces at 100 K (see above).

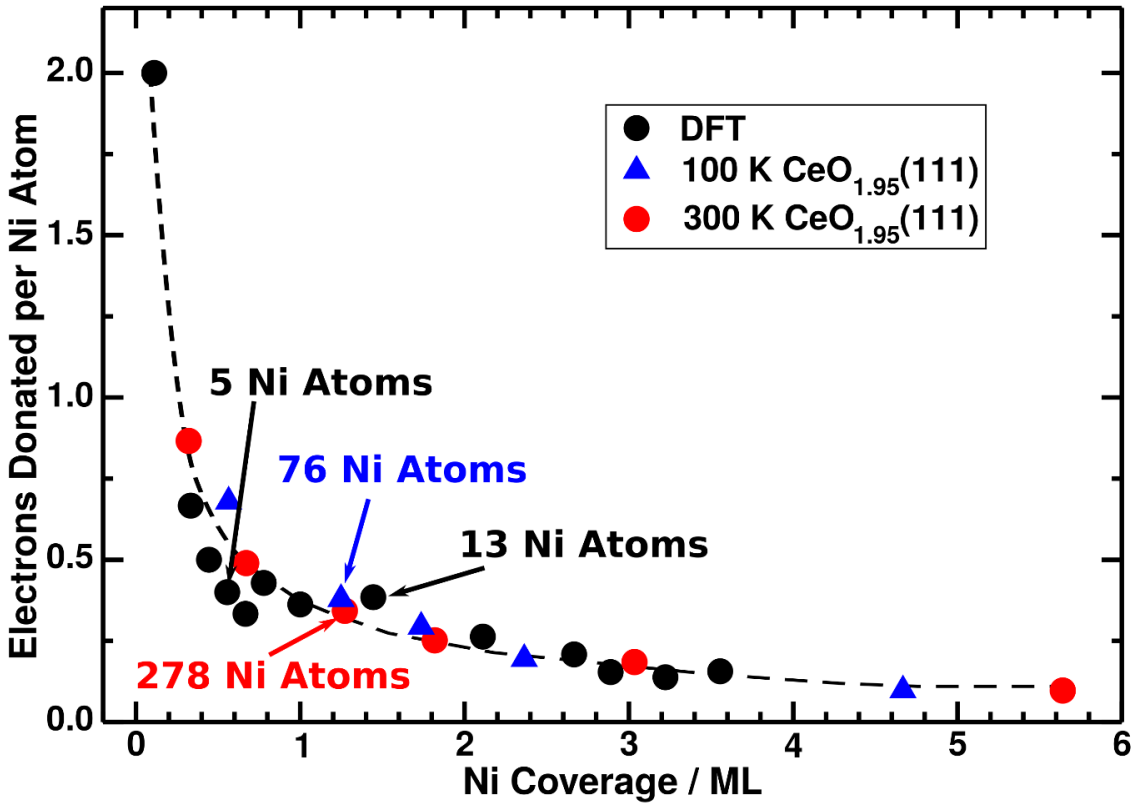

Figure 11. Number of electrons donated per Ni atom versus total Ni coverage, as calculated by DFT for CeO_2(111) and as measured for $CeO_{1.95}$(111) at 100 and 300 K. The numbers of atoms in the nanoparticles are also indicated for the points closest to 1.3 ML. The curve fit is just to guide the eye.

The experimental charge transfer at 300 K in Figure 11 is quite large. For example, for particles with 278 atoms, ~1/3 electron is transferred per Ni atom, so that the particle has a charge of +93. Since the aspect ratio of the particle is 0.25, about 1/3 of the Ni atoms are on the interface. Therefore, the measured total charge transfer will be realized if each Ni atom at the Ni-CeO_2 interface transfers one electron to the ceria. Apparently there is not too much Coulombic repulsion, because of attractions to the negative charge on the ceria (i.e., Ce^{3+} ions) at the interface, as indicated by the DFT calculations. The high strength of this interfacial bonding decreases the chemical potential of the Ni atoms in a way that can be directly related to the superior sinter resistance of these materials via well know rate equations.[76, 77]

The results above clearly show that the electronic character of the Ni atoms changes with Ni particle thickness and size, and with the location of the Ni atoms within the 3D particles (i.e., whether in the interfacial layer or in layers further away from the CeO_2 support), and with the extent of reduction of the CeO_2 support. We next show how these changes can be related to some of the unique catalytic properties of Ni/CeO_2 materials that have been reported, and how these vary with the structural properties of these materials at the atomic scale.

First, let us consider highly dispersed Ni on CeO_2 with few oxygen vacancies, where all the Ni atoms are either isolated monomers or small 2D clusters. We show above that these Ni atoms are highly cationic. It has been recently shown[6, 10-12] that well-dispersed, small Ni nanoparticles on a non-reduced ceria support, with all the Ni atoms being interfacial, promote the activation of both O–H and C–H bonds at room temperature, with lower activation barriers than for extended metallic Ni surfaces. Most importantly, this type of material can perform direct catalytic conversion of methane to methanol at low temperature (450 K), using a mixture of oxygen and water as the oxidant, with ~30% selectivity.[14] This we attribute to the highly cationic character of the surface Ni atoms. These same types of structural features were also reported to be most active for catalyzing the water-gas shift (WGS) reaction ($CO+ H_2O \rightarrow CO_2+H_2$), where higher Ni loadings (larger Ni particles) were shown to be less active.[1, 6]

For larger Ni nanoparticles, we find that *neutral* Ni atoms are above the oxidized interfacial Ni atoms and thus are exposed to gas-phase reactants. The calculated O–H bond cleavage activation energy at these neutral Ni atoms is higher than at the Ni monomers and few-atom Ni clusters discussed above, and not very different from that on Ni(111).[6] Hence, the Ni atoms at the rim of these larger nanoparticles are the only effective sites for O–H bond cleavage. These larger particles with both neutral Ni atoms and cationic Ni at the particle perimeters appear to be the most active for converting $CO+H_2O$ into methane.[1] In fact, the selectivity of $Ni/CeO_2(111)$ model catalysts was reported to depend strongly on Ni loading. Specifically, low-loaded systems catalyze the production of CO_2+H_2, whereas high-loaded systems catalyze the production of CH_4. The Ni loading also has a strong effect on the rate at which the system exposed to CH_4 deactivates: during dry reforming of methane on high-loaded systems, coke forms and deactivates the catalyst.[11]

The nature of the ceria support is also important. As discussed above, the binding of Ni nanoparticles on CeO_2 surfaces becomes increasingly weak as the degree of reduction of the ceria

surface increases; and, the amount of charge transferred from the Ni to the CeO_2, for the same small Ni particle size, also decreases strongly with the extent of reduction. Therefore, if operating conditions are changed for low-loaded Ni/CeO_2 catalysts in such a way that the CeO_2 gets more reduced, this will markedly reduce the charge on the Ni atoms. This is the case during methane dry reforming with CO_2 over low-loaded Ni/CeO_2 catalysts at 650 K.[10-12] The C–H cleavage barrier remains low even though, as we show above, the charge transfer from Ni to ceria is decreased due to ceria reduction, but now the C–O bond cleavage barrier in CO_2 also becomes low,[10] due to the presence of surface oxygen vacancies.

5. Conclusions

Ni atoms adsorb on slightly reduced ceria CeO_{2-x}(111) and form three-dimensional nanoparticles at 300 and 100 K, which increase in size with increasing Ni loading. The extent of reduction of ceria has a minor effect on the Ni particle number density at 300 K, while decreasing temperature from 300 to 100 K results in 3-fold higher Ni particle number density on $CeO_{1.95}$(111). The heat of Ni adsorption onto $CeO_{1.95}$(111) at 300 K starts from 345 kJ/mol (attributed to step edges), decreases within the first 0.2 ML to 323 kJ/mol (as step edge sites saturate), and increases afterward (due to growing particle size) until the bulk heat of Ni sublimation is reached by 9 ML. On $CeO_{1.8}$(111) at 300 K, this initial drop in heat of adsorption was not observed, attributed to weaker Ni binding to step edges when full of O vacancies. The heat of adsorption is generally lower on the more reduced ceria surface (by up to 65 kJ/mol initially at 300 K), again suggesting that the oxophilic Ni atoms do not prefer O vacancies. DFT calculations support this. On $CeO_{1.95}$(111) at 100 K, Ni atoms adsorb mainly on terraces due to slow Ni adatom diffusion, with an initial heat of adsorption that is 45 kJ/mol lower than that at 300 K where Ni atoms mainly adsorb on step edges. This highlights Ni's strong preference for step edges over terraces. Upon adsorption, Ni atoms donate electrons to the support to generate Ce^{3+}. DFT calculations show that this charge is localized on the interfacial Ni and Ce atoms in their atomic layers closest to the interface. As the coverage and particle size grow, the average number of electrons donated per Ni atom decreases in both experiments and DFT calculations. For the same size, Ni particles exhibit less charge transfer to $CeO_{1.95}$(111) at 100 K (when on terraces) than at 300 K (when at step edges). The charge transfer from Ni particles is much less on $CeO_{1.8}$(111) compared to $CeO_{1.95}$(111) at both temperatures.

Ni-CeO_2 interactions that produce strong electronic perturbations in the Ni nanoparticles result in important changes in their chemical and catalytic properties, as discussed for the examples of both O–H and C–H bond cleavage. Manipulating these interactions by, for example, controlling the degree of reduction of the support, as well as particle size and metal loading, can lead to improved catalytic activity and/or selectivity. Our findings help explain some of the outstanding catalytic properties of Ni/CeO_2 materials and how they depend upon their atomic-level structural details. This may aid in the rational design of catalysts that involve O–H and C–H bond dissociation.

ASSOCIATED CONTENT

Data availability

The DFT data that support the findings of this study are available in Materials Cloud {https://www.materialscloud.org/home} with the identifier doi:*****/materialscloud:2019.*****. The repository contains the calculations described in figures 7 to 11.

ACKNOWLEDGEMENTS

The authors (C.T.C. and Z.M.) acknowledge the Department of Energy, Office of Basic Energy Sciences, Chemical Sciences Division grant number DE-FG02-96ER14630, for support of this work. This project also received funding from the European Union's Horizon 2020 research and innovation programme under the Marie Skłodowska-Curie grant agreement No 832121. Computer time provided by the BIFI-ZCAM, the RES (Red Española de Supercomputación) resources at MareNostrum 4 (BSC, Barcelona) and Altamira (IFCA, Cantabria) nodes, the Piluso node within SNCAD (Sistema Nacional de Computación de Alto Desempeño, Argentina), is acknowledged. Computer time provided by the DECI resources at Finis Terrae II based in Spain at CESGA, with the support from PRACE aislb, is also acknowledge. M.V.G.P. thanks the support by the MINECO and MICINN-Spain (CTQ2015-71823-R and RTI2018-101604-B-I00, respectively).

References

1. Senanayake, S. D.; Evans, J.; Agnoli, S.; Barrio, L.; Chen, T. L.; Hrbek, J.; Rodriguez, J. A., Water-Gas Shift and CO Methanation Reactions over Ni-CeO_2(111) Catalysts. *Top. Catal.* **2011,** *54*, 34-41.
2. Carrasco, J.; Barrio, L.; Liu, P.; Rodriguez, J. A.; Ganduglia-Pirovano, M. V., Theoretical Studies of the Adsorption of CO and C on Ni(111) and Ni/CeO_2 (111): Evidence of a Strong Metal-Support Interaction. *J. Phys. Chem. C* **2013,** *117*, 8241-8250.
3. Senanayake, S. D.; Rodriguez, J. A.; Stacchiola, D., Electronic Metal-Support Interactions and the Production of Hydrogen Through the Water-Gas Shift Reaction and Ethanol Steam Reforming: Fundamental Studies with Well-Defined Model Catalysts. *Top. Catal.* **2013,** *56*, 1488-1498.
4. Xu, W. Q.; Liu, Z. Y.; Johnston-Peck, A. C.; Senanayake, S. D.; Zhou, G.; Stacchiola, D.; Stach, E. A.; Rodriguez, J. A., Steam Reforming of Ethanol on Ni/CeO_2: Reaction Pathway and Interaction between Ni and the CeO_2 Support. *ACS Catal.* **2013,** *3*, 975-984.
5. Rodriguez, J. A.; Xu, W. Q.; Liu, Z. Y.; Senanayake, S.; Stacchiola, D., Steam Reforming of Ethanol on Ni-Ce-O Catalysts: Reaction Pathway and Interaction Between Ni and the CeO_2 Components. *Abstracts of Papers of the American Chemical Society* **2014,** *248*.
6. Carrasco, J.; Lopez-Duran, D.; Liu, Z. Y.; Duchon, T.; Evans, J.; Senanayake, S. D.; Crumlin, E. J.; Matolin, V.; Rodriguez, J. A.; Ganduglia-Pirovano, M. V., In Situ and Theoretical Studies for the Dissociation of Water on an Active Ni/CeO_2 Catalyst: Importance of Strong Metal-Support Interactions for the Cleavage of O-H Bonds. *Angew. Chem., Int. Ed.* **2015,** *54*, 3917-3921.
7. Ganduglia-Pirovano, M. V., The Non-Innocent Role of Cerium Oxide in Heterogeneous Catalysis: A Theoretical Perspective. *Catal. Today* **2015,** *253*, 20-32.
8. Liu, Z. Y.; Duchon, T.; Wang, H. R.; Peterson, E. W.; Zhou, Y. H.; Luo, S.; Zhou, J.; Matolin, V.; Stacchiola, D. J.; Rodriguez, J. A.; Senanayake, S. D., Mechanistic Insights of Ethanol Steam Reforming over Ni-CeO_x(111): The Importance of Hydroxyl Groups for Suppressing Coke Formation. *J. Phys. Chem. C* **2015,** *119*, 18248-18256.
9. Liu, Z. Y.; Duchon, T.; Wang, H. R.; Grinter, D. C.; Waluyo, I.; Zhou, J.; Liu, Q.; Jeong, B.; Crumlin, E. J.; Matolin, V.; Stacchiola, D. J.; Rodriguez, J. A.; Senanayake, S. D., Ambient Pressure XPS and IRRAS Investigation of Ethanol Steam Reforming on Ni-CeO_2(111) Catalysts: an In Si tu Study of C-C and O-H Bond Scission. *Phys. Chem. Chem. Phys.* **2016,** *18*, 16621-16628.
10. Liu, Z. Y.; Grinter, D. C.; Lustemberg, P. G.; Nguyen-Phan, T. D.; Zhou, Y. H.; Luo, S.; Waluyo, I.; Crumlin, E. J.; Stacchiola, D. J.; Zhou, J.; Carrasco, J.; Busnengo, H. F.; Ganduglia-Pirovano, M. V.; Senanayake, S. D.; Rodriguez, J. A., Dry Reforming of Methane on a Highly-Active Ni-CeO_2 Catalyst: Effects of Metal-Support Interactions on C-H Bond Breaking. *Angew. Chem., Int. Ed.* **2016,** *55* , 7455-7459.
11. Lustemberg, P. G.; Ramirez, P. J.; Liu, Z. Y.; Gutierrez, R. A.; Grinter, D. G.; Carrasco, J.; Senanayake, S. D.; Rodriguez, J. A.; Ganduglia-Pirovano, M. V., Room-Temperature Activation of Methane and Dry Re-forming with CO_2 on Ni-CeO_2(111) Surfaces: Effect of Ce^{3+} Sites and Metal-Support Interactions on C-H Bond Cleavage. *ACS Catal.* **2016,** *6*, 8184-8191.
12. Liu, Z. Y.; Lustemberg, P.; Gutierrez, R. A.; Carey, J. J.; Palomino, R. M.; Vorokhta, M.; Grinter, D. C.; Ramirez, P. J.; Matolin, V.; Nolan, M.; Ganduglia-Pirovano, M. V.; Senanayake, S. D.; Rodriguez, J. A., In Situ Investigation of Methane Dry Reforming on Metal/Ceria(111) Surfaces: Metal-Support Interactions and C-H Bond Activation at Low Temperature. *Angew. Chem., Int. Ed.* **2017,** *56*, 13041-13046.
13. Liu, Z. Y.; Yao, S. Y.; Johnston-Peck, A.; Xu, W. Q.; Rodriguez, J. A.; Senanayake, S. D., Methanol Steam Reforming over Ni-CeO_2 Model and Powder Catalysts: Pathways to High Stability and Selectivity for H_2/CO_2 Production. *Catal. Today* **2018,** *311*, 74-80.
14. Lustemberg, P. G.; Palomino, R. M.; Gutierrez, R. A.; Grinter, D. C.; Vorokhta, M.; Liu, Z. Y.; Ramirez, P. J.; Matolin, V.; Ganduglia-Pirovano, M. V.; Senanayake, S. D.; Rodriguez, J. A., Direct

Conversion of Methane to Methanol on Ni-Ceria Surfaces: Metal-Support Interactions and Water-Enabled Catalytic Conversion by Site Blocking. *J. Am. Chem. Soc.* **2018,** *140*, 7681-7687.
15. Voychok, D.; Guild, C. J.; Llorca, J.; Palomino, R. M.; Waluyo, I.; Rodriguez, J. A.; Suib, S. L.; Senanayake, S. D., Structural and Chemical State of Doped and Impregnated Mesoporous Ni/CeO_2 Catalysts for the Water-Gas Shift. *Appl. Catal., A* **2018,** *567*, 1-11.
16. Lustemberg, P. G.; Feria, L.; Ganduglia-Pirovano, M. V., Single Ni Sites Supported on CeO_2 (111) Reveal Cooperative Effects in the Water-Gas Shift Reaction. *J. Phys. Chem. C* **2019,** *123*, 7749-7757.
17. Akri, M.; Zhao, S.; Li, X.; Zang, K.; Lee, A. F.; Isaacs, M. A.; Xi, W.; Gangarajula, Y.; Luo, J.; Ren, Y.; Cui, Y.; Li, L.; Su, Y.; Pan, X.; Wen, W.; Pan, Y.; Wilson, K.; Qiao, B.; Ishii, H.; Liao, Y.; Wang, A.; Wang, X.; Zhang, T., Atomically Dispersed Nickel as Coke-Resistant Active Sites for Methane Dry Reforming. *Nat. Commun.* **2019,** *10*, 1-10.
18. Farrauto, R.; Hwang, S.; Shore, L.; Ruettinger, W.; Lampert, J.; Giroux, T.; Liu, Y.; Ilinich, O., New Material Needs for Hydrocarbon Fuel Processing: Generating Hydrogen for the PEM Fuel Cell. *Annu. Rev. Mater. Res.* **2003,** *33*, 1-27.
19. Campbell, C. T.; Peden, C. H. F., Chemistry - Oxygen Vacancies and Catalysis on Ceria Surfaces. *Science* **2005,** *309*, 713-714.
20. Rocchini, E.; Trovarelli, A.; Llorca, J.; Graham, G. W.; Weber, W. H.; Maciejewski, M.; Baiker, A., Relationships between Structural/Morphological Modifications and Oxygen Storage-Redox Behavior of Silica Ceria. *J. Catal.* **2000,** *194*, 461-78.
21. Farmer, J. A.; Campbell, C. T., Ceria Maintains Smaller Metal Catalyst Particles by Strong Metal-Support Bonding. *Science* **2010,** *329*, 933-936.
22. Kundakovic, L.; Flyzani-Stephanopoulos, J., Cu and Ag-Modified Cerium Oxide Catalysts for Methane Oxidation. *J. Catal.* **1998,** *179*, 203-21.
23. Schwartz, J. M.; Schmidt, L. D., Microstructures of Pt-Ce and Rh-Ce Particles on Alumina and Silica. *J. Catal.* **1992,** *138*, 283-93.
24. Campbell, C. T., The Energetics of Supported Metal Nanoparticles: Relationships to Sintering Rates and Catalytic Activity. *Acc. Chem. Res.* **2013,** *46*, 1712-1719.
25. Sellers, J. R. V.; James, T. E.; Hemmingson, S. L.; Farmer, J. A.; Campbell, C. T., Adsorption Calorimetry during Metal Vapor Deposition on Single Crystal Surfaces: Increased Flux, Reduced Optical Radiation, and Real-Time Flux and Reflectivity Measurements. *Rev. Sci. Instrum.* **2013,** *84*, 123901.
26. James, T. E.; Hemmingson, S. L.; Ito, T.; Campbell, C. T., Energetics of Cu Adsorption and Adhesion onto Reduced CeO_2(111) Surfaces by Calorimetry. *J. Phys. Chem. C* **2015,** *119*, 17209-17217.
27. James, T. E.; Hemmingson, S. L.; Campbell, C. T., Energy of Supported Metal Catalysts: From Single Atoms to Large Metal Nanoparticles. *ACS Catal.* **2015,** *5*, 5673-5678.
28. Hemmingson, S. L.; James, T. E.; Feeley, G. M.; Tilson, A. M.; Campbell, C. T., Adsorption and Adhesion of Au on Reduced CeO_2 (111) Surfaces at 300 and 100 K. *J. Phys. Chem. C* **2016,** *120*, 12113-12124.
29. Farmer, J. A.; Baricuatro, J. H.; Campbell, C. T., Ag Adsorption on Reduced CeO_2 (111) Thin Films. *J. Phys. Chem. C* **2010,** *114*, 17166-17172.
30. Wilson, E. L.; Brown, W. A.; Thornton, G., RAIRS Studies of CO Adsorption on Pd/$CeO_{(2-x)}$(111)/Pt(111). *Surf. Sci.* **2006,** *600*, 2555-2561.
31. Stuckless, J. T.; Frei, N. A.; Campbell, C. T., A Novel Single-Crystal Adsorption Calorimeter and Additions for Determining Metal Adsorption and Adhesion Energies. *Rev. Sci. Instrum.* **1998,** *69*, 2427-2438.
32. Campbell, C. T.; James, T. E., Ion Scattering Spectroscopy Intensities for Supported Nanoparticles: The Hemispherical Cap Model. *Surf. Sci.* **2015,** *641*, 166-169.
33. Kresse, G.; Hafner, J., Ab Initio Molecular-Dynamics for Liquid-Metals. *Phys. Rev. B* **1993,** *47*, 558–561.

34. Kresse, G.; Furthmüller, J., Efficient Iterative Schemes for Ab Initio Total-Energy Calculations Using a Plane-Wave Basis Set. *Phys. Rev. B* **1996,** *54*, 11169.
35. Kresse, G.; Joubert, D., From Ultrasoft Pseudopotentials to the Projector Augmented-Wave Method. *Phys. Rev. B* **1999,** *59*, 1758–1775.
36. Dudarev, S. L.; Botton, G. A.; Savrasov, S. Y.; Humphreys, C. J.; Sutton, A. P., Electron-Energy-Loss Spectra and the Structural Stability of Nickel Oxide: An LSDA+U Study. *Phys. Rev. B* **1998,** *57*, 1505-1509.
37. Perdew, J. P.; Burke, K.; Ernzerhof, M., Generalized Gradient Approximation Made Simple. *Phys. Rev. Lett.* **1996,** *77*, 3865-3868.
38. Fabris, S.; Vicario, G.; Balducci, G.; de Gironcoli, S.; Baroni, S., Electronic and Atomistic Structures of Clean and Reduced Ceria Surfaces. *J. Phys. Chem. B* **2005,** *109*, 22860-22867.
39. Castleton, C. W. M.; Kullgren, J.; Hermansson, K., Tuning LDA+U for Electron Localization and Structure at Oxygen Vacancies in Ceria. **2007,** *127*, 244704.
40. Andersson, D. A.; Simak, S. I.; Johansson, B.; Abrikosov, I. A.; Skorodumova, N. V., Modeling of CeO_2, Ce_2O_3, and CeO_{2-x} in the LDA+U Formalism. *Phys. Rev. B* **2007,** *75*, 035109.
41. Da Silva, J. L. F.; Ganduglia-Pirovano, M. V.; Sauer, J.; Bayer, V.; Kresse, G., Hybrid Functionals Applied to Rare-Earth Oxides: The Example of Ceria. *Phys. Rev. B* **2007,** *75*, 045121.
42. Du, D.; Wolf, M. J.; Hermansson, K.; Broqvist, P., Screened Hybrid Functionals Applied to Ceria: Effect of Fock Exchange. *Phys. Rev. B* **2018,** *97*, 235203.
43. Loschen, C.; Carrasco, J.; Neyman, K. M.; Illas, F., First-Principles LDA + U and GGA + U Study of Cerium Oxides: Dependence on the Effective U Parameter. *Phys. Rev. B* **2007,** *75*, 035115.
44. Grimme, S.; Antony, J.; Ehrlich, S.; Krieg, H., A Consistent and Accurate Ab Initio Parametrization of Density Functional Dispersion Correction (DFT-D) for the 94 Elements H-Pu. *J. Chem. Phys.* **2010,** *132*, 154104.
45. Grimme, S.; Ehrlich, S.; Goerigk, L., Effect of the Damping Function in Dispersion Corrected Density Functional Theory. *J. Comput. Chem.* **2011,** *32*, 1456-1465.
46. Zhou, Y.; Perket, J. M.; Crooks, A. B.; Zhou, J., Effect of Ceria Support on the Structure of Ni Nanoparticles. *J. Phys. Chem. Lett.* **2010,** *1*, 1447-1453.
47. Venables, J. A., Atomic Processes in Crystal Growth. *Surface Sci.* **1994,** *299/300*, 798.
48. Zhou, Y. H.; Perket, J. M.; Crooks, A. B.; Zhou, J., Effect of Ceria Support on the Structure of Ni Nanoparticles. *J. Phys. Chem. Lett.* **2010,** *1*, 1447-1453.
49. Castellani, N. J.; Branda, M. A.; Neyman, K. M.; Illas, F., Density Functional Theory Study of the Adsorption of Au Atom on Cerium Oxide: Effect of Low-Coordinated Surface Sites. *J. Phys. Chem. C* **2009,** *113*, 4948-4954.
50. Hernandez, N. C.; Grau-Crespo, R.; de Leeuw, N. H.; Sanz, J. F., Electronic Charge Transfer between Ceria Surfaces and Gold Adatoms: A GGA Plus U Investigation. *Phys. Chem. Chem. Phys.* **2009,** *11*, 5246-5252.
51. Zhang, C.; Michaelides, A.; King, D. A.; Jenkins, S. J., Structure of Gold Atoms on Stoichiometric and Defective Ceria Surfaces. *J. Chem. Phys.* **2008,** *129*, 194780.
52. Zhang, C. J.; Michaelides, A.; King, D. A.; Jenkins, S. J., Anchoring Sites for Initial Au Nucleation on CeO_2{111}: O Vacancy versus Ce Vacancy. *J. Phys. Chem. C* **2009,** *113* (16), 6411-6417.
53. Camellone, M. F.; Fabris, S., Reaction Mechanisms for the CO Oxidation on Au/CeO_2 Catalysts: Activity of Substitutional Au^{3+}/Au^{+} Cations and Deactivation of Supported Au^{+} Adatoms.*J. Am. Chem. Soc.* **2009,** *131*, 10473-10483.
54. Lustemberg, P. G.; Pan, Y.; Shaw, B. J.; Grinter, D.; Pang, C.; Thornton, G.; Pérez, R.; Ganduglia-Pirovano, M. V.; Nilius, N., Diffusion Barriers Block Defect Occupation on Reduced CeO_2(111). *Phys. Rev. Lett.* **2016,** *116*, 236101.

55. Pan, Y.; Nilius, N.; Freund, H. J.; Paier, J.; Penschke, C.; Sauer, J., Titration of Ce^{3+} Ions in the CeO_2(111) Surface by Au Adatoms. *Phys. Rev. Lett.* **2013,** *111*, 206101.
56. Rodriguez, J. A.; Wang, X.; Liu, P.; Wen, W.; Hanson, J. C.; Hrbek, J.; Perez, M.; Evans, J., Gold Nanoparticles on Ceria: Importance of O Vacancies in the Activation of Gold. *Top. Catal.* **2007,** *44* , 73-81.
57. Pan, Y.; Cui, Y.; Stiehler, C.; Nilius, N.; Freund, H. J., Gold Adsorption on CeO_2 Thin Films Grown on Ru(0001). *J. Phys. Chem. C* **2013,** *117*, 21879-21885.
58. Rodriguez, J.; Perez, M.; Evans, J.; Liu, G.; Hrbek, J., Reaction of SO_2 with Au/CeO_2(111): Importance of O Vacancies in the Activation of Gold. *J. Chem. Phys.* **2005,** *122*, 241101.
59. Kozlov, S. M.; Neyman, K. M., O Vacancies on Steps on the CeO_2(111) Surface. *Phys. Chem. Chem. Phys.* **2014,** *16*, 7823-7829.
60. Campbell, C. T.; Sellers, J. R. V., Anchored Metal Nanoparticles: Effects of Support and Size on Their Energy, Sintering Resistance and Reactivity. *Faraday Discuss.* **2013,** *162*, 9-30.
61. Romeo, M.; Bak, K.; El Fallah, J.; Lenormand, F.; Hilaire, L., XPS Study of the Reduction of Cerium Dioxide. *Surf. Interface Anal.* **1993,** *20*, 508-512.
62. Tanuma, S.; Powell, C. J.; Penn, D. R., Calculations of Electron Inelastic Mean Free Paths for 31 Materials. *Surf. Interface Anal.* **1988,** *11*, 577-589.
63. Grosvenor, A. P.; Biesinger, M. C.; Smart, R. S.; McIntyre, N. S., New Interpretations of XPS Spectra of Nickel Metal and Oxides. *Surf. Sci.* **2006,** *600*, 1771-1779.
64. Zhou, Y. H.; Zhou, J., Interactions of Ni Nanoparticles with Reducible CeO_2(111) Thin Films. *J. Phys. Chem. C* **2012,** *116*, 9544-9549.
65. Monkhorst, H. J.; Pack, J. D., Special Points for Brillouin-Zone Integrations. *Phys. Rev. B* **1976,** *13*, 5188-5192.
66. Tang, W.; Sanville, E.; Henkelman, G., A Grid-Based Bader Analysis Algorithm without Lattice Bias. *Journal of Physics: Condens. Matter* **2009,** *21*, 084204.
67. Janthon, P.; Luo, S.; Kozlov, S. M.; Viñes, F.; Limtrakul, J.; Truhlar, D. G.; Illas, F., Bulk Properties of Transition Metals: A Challenge for the Design of Universal Density Functionals. *J. Chem. Theory. Comput.* **2014,** *10*, 3832-3839.
68. Zhang, G.-X.; Reilly, A. M.; Tkatchenko, A.; Scheffler, M., Performance of Various Density-Functional Approximations for Cohesive Properties of 64 Bulk Solids. *New J. Phys.* **2018,** *20*, 063020.
69. Kim, H. Y.; Henkelman, G., CO Oxidation at the Interface of Au Nanoclusters and the Stepped-CeO_2(111) Surface by the Mars-van Krevelen Mechanism. *J. Phys. Chem. Lett.* **2013,** *4*, 216-221.
70. Ganduglia-Pirovano, M. V.; Hofmann, A.; Sauer, J., Oxygen Vacancies in Transition Metal and Rare Earth Oxides: Current State of Understanding and Remaining Challenges. *Surf. Sci. Reports* **2007,** *62*, 219-270.
71. Murgida, G. E.; Ganduglia-Pirovano, M. V., Evidence for Subsurface Ordering of Oxygen Vacancies on the Reduced CeO_2(111) Surface Using Density-Functional and Statistical Calculations. *Phys. Rev. Lett.* **2013,** *110*, 246101.
72. Han, Z.-K.; Yang, Y.-Z.; Zhu, B.; Ganduglia-Pirovano, M. V.; Gao, Y., Unraveling the Oxygen Vacancy Structures at the Reduced CeO_2(111) Surface. *Phys. Rev. Mater.* **2018,** *2*, 035802.
73. Paier, J.; Penschke, C.; Sauer, J., Oxygen Defects and Surface Chemistry of Ceria: Quantum Chemical Studies Compared to Experiment. *Chem. Rev.* **2013,** *113*, 3949-3985.
74. Hailstone, R. K.; DiFrancesco, A. G.; Leong, J. G.; Allston, T. D.; Reed, K. J., A Study of Lattice Expansion in CeO_2 Nanoparticles by Transmission Electron Microscopy. *The J. Phys. Chem. C* **2009,** *113*, 15155-15159.
75. Campbell, C. T., Bimetallic Surface Chemistry. *Annu. Rev. Phys. Chem.* **1990,** *41*, 775-837.
76. Campbell, C. T.; Parker, S. C.; Starr, D. E., The Effect of Size-Dependent Nanoparticle Energetics on Catalyst Sintering. *Science* **2002,** *298*, 811-814.

77. Parker, S. C.; Campbell, C. T., Kinetic Model for Sintering of Supported Metal Particles with Improved Size-Dependent Energetics and Applications to Au on TiO_2(110). *Phys. Rev. B* **2007,** *75*, 035430.

Table of Contents Image: